Supplementary Information

Dredging photocarrier trapping pathways via "charge bridge" driven exciton-phonon decoupling enables efficient and photothermal stable quaternary organic solar cells

Kangning Zhang,[a] Zhinan Jiang,[b] Jiawei Qiao,[a] Peng Lu,[c] Chaochao Qin,[b] Hang Yin,[a] Xiaoyan Du,[a] Wei Qin,[a] Xiaotao Hao*[ad]

[a]School of Physics, State Key Laboratory of Crystal Materials, Shandong University, Jinan, Shandong 250100, P. R. China
E-mail: haoxt@sdu.edu.cn

[b]Henan Key Laboratory of Infrared Materials & Spectrum Measures and Applications, Henan Normal University, Xinxiang, Henan 453007, P. R. China

[c]School of Physics, National Demonstration Center for Experimental Physics Education, Shandong University, Jinan, Shandong 250100, P. R. China

[d]ARC Centre of Excellence in Exciton Science, School of Chemistry, The University of Melbourne, Parkville, Victoria 3010, Australia

1. Experimental Section

1.1 Materials

Commercial indium tin oxide (ITO) with dimensions of 16.1×16.1 mm was purchased from South China Science & Technology Company Limited. PM6, PB2F, BTP-eC9, L8-BO, PY-IT and PNDIT-F3N were purchased from Solarmer Materials (Beijing) Inc. PEDOT:PSS (Clevios PVP Al 4083) was purchased from Xi'an Polymer Light Technology Corp. V_2O_5 and LiF were supplied by Shanghai Aladdin Biochemical Technology Co., Ltd. Chloroform (CF), *o*-xylene (*o*-XY), methanol and 1,8-Diiodooctane (DIO) were purchased from Sigma Aldrich. All the materials were used as received without purification.

1.2 Solar Cells Preparation

Solar cells with the ITO/V_2O_5/PEDOT:PSS/Active layer/LiF/PNDIT-F3N/Ag configuration were fabricated according to the following procedure. ITO glass was first washed with detergent

and then ultrasonic washed with deionized water, acetone, ethanol and isopropanol for 20 min each. After 15 min cleaned with ultraviolet ozone, the prepared V_2O_5 solution was spin coated on the ITO substrate at 2000 rpm for 50 s. Then the ITO/V_2O_5 substrate was placed on the hot-plate and annealed at 150 °C for 5 min in air to generate the V_2O_5 layer. Before the active layer fabrication, the PEDOT:PSS (Clevios PVP Al 4083) solution was deposited onto the ITO/V_2O_5 substrate at 4000 rpm for 50 s and baked at 150 °C for 15 min under ambient conditions. The PM6:BTP-eC9 blend solution (1:1.2, wt%, 17.6 mg ml^{-1} in CF or o-XY with 0.5% DIO) was prepared and stirred at 50 °C for at least 2 h in CF or 80 °C for at least 12 h in o-XY. The ternary blend solution was obtained by adjusting the doping ratio of L8-BO in acceptor. Moreover, the corresponding quaternary blend solution was obtained by adjusting the doping ratio of PY-IT in acceptor and PB2F in donor. The PM6:BTP-eC9-based binary, ternary and quaternary blend solution was spin-coated on the top of the ITO/V_2O_5/PEDOT:PSS substrate at 4000 rpm for 30 s and treated with thermal annealing at 100 °C for 10 min in a high-purity N_2-filled glove box to form the photoactive layer of ~110 nm. Subsequently, a 1 nm LiF layer was deposited by thermal evaporation on the top of the photoactive layer and a 5 nm PNDIT-F3N (1 mg ml^{-1} in methanol) layer was spin-coated on the top of LiF layer at 3000 rpm for 30 s. Finally, a 100 nm Ag electrode layer was deposited under high vacuum in an evaporation chamber. The active area of organic solar cells defined by a shadow mask is ~4 mm^2.

As for single-carrier device fabrication, The hole-only OPV devices were fabricated with a structure of ITO/V_2O_5/PEDOT:PSS/photoactive layer/MoO_3/Ag. A 7.5 nm MoO_3 layer was thermally evaporated on the top of the photoactive layer. The electron-only OPV devices were fabricated with a structure of ITO/ZnO/photoactive layer/LiF/PNDIT-F3N/Ag. The precursor solution of ZnO was spin-coated on the patterned ITO substrate at 4000 rpm for 50 s and baked under 200 °C for 1 h under ambient conditions. The thickness of the photoactive layer of single-carrier devices is ~110 nm.

1.3 Solar Cells Measurement

The J-V measurements of solar cells were performed in an N_2-filled glove box by empolying a computer-controlled Keithley 2400 source under the illumination of AM 1.5G irradiation (100 mW cm^{-2}) with a simulated solar simulator (SOFN INSTRUMENTS CO., LTD) at room temperature. The standard monosilicon solar cell was used to calibrate irradiation intensity of the simulated solar simulator. The EQE spectra was measured with a commercial 7-SCSpec test system. The encapsulated solar cells were fabricated to conduct the photothermal stability measurements under continuous illumination of a 100 mW cm^{-2} white LED at 50-55 °C. The

FTPS-EQE measurements were carried out by empolying a Fourier-transform infrared (FTIR) spectrometer equipped with a halogen lamp light source and an external detector option. As for single-carrier device measurements, the dark current characteristics of hole-only and electron-only OPV devices under forward bias were extracted to obtain carrier mobilities according to the space-charge-limited current (SCLC) method by the following equation,

$$J \times d = \frac{9}{8}\varepsilon_0\varepsilon_r\mu_0 exp(0.89\beta\sqrt{F})F^2$$

where J is the current density, d is the thickness of the photoactive layer, ε_0 is the permittivity under vacuum (8.85×10^{-14} F/cm), ε_r is the average dielectric constant of the photoactive layer (3), μ_0 is the zero-field hole or electron mobility, β is the Poole-Frankel (PF) slope, F is the applied electric field. In addition, the single-carrier OPV devices were encapsulated in a high-purity N_2-filled glove box for the temperature-dependent carrier mobility measurements.

1.4 Characterization

UV-vis absorption spectra were measured on an Agilent Cary 5000 spectrophotometer with films on the quartz plates at room temperature. Ultraviolet photoelectron spectrometer (UPS) measurement was performed by an PHI5000 VersaProbe III (Scanning ESCA Microprobe) and SCA (Spherical Analyzer). Molecular weights and polydispersity indexes of polymers were determined by high temperature (150 ℃) gel permeation chromatography (GPC) method. AFM measurement was conducted by a Nano Scope IIIA instrument in the tapping mode. The GIWAXS characterization of the thin-films was performed at BL16B1 beamline at Shanghai Synchrotron Radiation Facility (SSRF), China. The distance of sample-to-detector, incidence light angle and wavelength are 268 mm, 0.15° and 0.124 nm, respectively. GIWAXS samples were prepared under device conditions on the Si/PEDOT:PSS substrates. The d-spacing is the π-π stacking distance calculated from d-spacing $= 2\pi/q_{z(010)}$. The CCL value is calculated from the Scherrer equation: $CCL = 2\pi k$/FWHM, where k and FWHM are the Scherrer constant of 0.9 and the full width at half the maximum (FWHM) of (010) π-π stacking peaks in the out-of-plane direction, respectively. Temperature-dependent PL measurements for the encapsulated thin-films were performed with a spectrometer (PG2000 Pro, Fuxiang Inc.) from fluorescence lifetime imaging microscopy (FLIM). The Ti:sapphire amplifier (Astrella, Coherent) supplies 800 nm pulse to excite the encapsulated samples and generate the PL signals. The liquid nitrogen cooling chamber (TC280, East Changing, Inc.) was used to modulate the target temperature during the test. TRPL measurements were conducted through a laser-scanned confocal imaging microscopy (Nanofinder FLEX2, Tokyo Instruments, Inc.) combined with a time-correlated single-photon counting (TCSPC) module (Becker & Hickl, SPC-150). Contact

angle images were recorded through a contact angle meter (Dataphysics OCA40). Impedance spectroscopy (IS) measurements of the encapsulated OSCs were carried out with an impedance analyzer (E4990A). Femtosecond transient absorption (TA) spectroscopy measurements were performed with an Ultrafast Helios pump-probe optical system combined with a regenerative amplified Ti:sapphire laser system from Coherent (800 nm, 100 fs, 7 mJ/pluse, 1 KHz repetition rate). The maximum delay time of femtosecond TA spectroscopy equipment is about 8 ns.

1.5 Phase Distribution Measurement

The surface tensions of the donor and acceptor materials are calculated from contact angle measurements according to the equation[1] of

$$\gamma_{sol}(1 + cos\theta) = 2\sqrt{\gamma_{sol}^d \gamma^d} + 2\sqrt{\gamma_{sol}^p \gamma^p}$$

where γ_{sol} is the surface tension, γ_{sol}^d and γ_{sol}^p are the dispersion and polar components of surface tensions, respectively, θ is the contact angle.

The Flory-Huggins interaction parameter χ between the materials X and Y is employed to describe quantitatively their miscibility as below,

$$\chi \propto (\sqrt{\gamma_X} - \sqrt{\gamma_Y})^2$$

where γ_X and γ_Y are the surface tension of the materials (X and Y), respectively.

The interfacial tension between materials X and Y can be evaluated by the Wu's equation,[2]

$$\gamma_{XY} = \gamma_X + \gamma_Y - \frac{4\gamma_X^d \gamma_Y^d}{\gamma_X^d + \gamma_Y^d} - \frac{4\gamma_X^p \gamma_Y^p}{\gamma_X^p + \gamma_Y^p}$$

where γ_{XY} is the interfacial tension between the materials X and Y, γ_i is the surface tension of the material i, where i = X or Y, and as γ_i^d and γ_i^p are the dispersion and polar components of γ_i.

The wetting coefficient (ω) of the extra component X in the donor:acceptor (D:A) blend can be expressed according to Young's equation[3] of

$$\omega_X = \frac{\gamma_{A/X} - \gamma_{D/X}}{\gamma_{D/A}}$$

if ω is smaller than -1, X will infuse into the phase of A. if ω is larger than 1, X will infuse into the phase of D. If -1 < ω < 1, X will be located at the interfaces of D and A.

1.6 Exciton Annihilation and Trapping Measurement

The depopulation of the excited state is most clearly studied by examining the photoinduced absorption (PIA) kinetics, which is a positive signal coming from the increased absorption from the excited state into the higher-lying states. Herein, the PIA kinetics of singlet excitons were

fitted according to an exciton-exciton annihilation model accounting for both long-range and collisional mechanisms,[4] that is,

$$\frac{dN}{dt} = G(t) - \frac{N}{\tau} - \beta N^2 - \frac{\gamma}{t^d}N^2$$

where $N(t)$ represents the time-dependent exciton number per volume (m^{-3}), $G(t)$ represents the rate of exciton generation under excitation pulse, τ represents the exciton decay lifetime without annihilation. Especially, the term βN^2 represents the rate of collisional annihilation, where β is the collisional coefficient. Furthermore, the final term $(\gamma/t^d)N^2$ represents the rate of long-range annihilation induced by Förster resonance energy transfer (FRET) between point dipoles, where γ is the long-range annihilation coefficient.

In general, when excitation pulse is in the form of a Gaussian profile, $G(t)$ can be calculated from the following equation

$$G(t) = \frac{\epsilon P c}{A_p E_{ph}} \frac{exp\left[-(t - t_0)^2/2\sigma_t^2 \right]}{\left(2\pi\sigma_t^2\right)^{1/2}}$$

herein, ε represents the ground-state extinction coefficient (mol^{-1} m^2), P represents the pump pulse energy (J), c represents the ground-state concentration of exciton sites (mol m^{-3}), A_p represents the spot area of pump beam (m^2), E_{ph} ($h\upsilon$) represents the wavelength-dependent single-photon energy (J), t_0 represents the center of pump pulse, and σ_t represents the width of pump pulse. Therefore, the initial density of excitons (m^{-3}) photogenerated by one pump pulse was defined as the Gaussian coefficient $N_0 = \varepsilon P c/A_p E_{ph}$.

The three-dimensional diffusion and collisional annihilation of excitons was described by the following model:

$$\frac{dN}{dt} = -8\pi D a N^2(t) + \frac{8\pi D a^2 N^2(t)}{\sqrt{2\pi D}\ \sqrt{t}}$$

where D represents the diffusion coefficient of singlet excitons (cm^2 s^{-1}), a represents the critical distance of the collisional annihilation.

Exciton annihilation originating from single-step FRET between homogeneously distributed point dipoles was described by the following model:

$$\frac{dN}{dt} = -\frac{2}{3}\pi^{3/2}\tau^{-1/2}R_F^3\frac{N^2(t)}{\sqrt{t}}$$

where R_F represents the Förster radius.

1.7 Polaron Trapping and Detrapping Measurement

The residual charge recombination model was employed to quantify polaron trapping and detrapping dynamics,[5] that is,

$$\frac{dn}{dt} = Nk_T - n\sum_j K_j$$

where n is the polaron density, N is the trapped polaron density, k_T is the rate constant of polaron detrapping, K_j is the rate constant of radiative and non-radiative recombination. Herein, k_T was obtained from the Arrhenius equation as follows,

$$k_T = S exp(-\frac{E}{k_B T})$$

herein, E is the thermal activation energy, S is the frequency factor. Noted that two processes account for the kinetics of trapped polarons described by

$$\frac{dN}{dt} = -N_0 S exp(-\frac{E}{k_0 T})$$

$$N(t) = N_0 exp(-k_T t)$$

where N_0 is the initial trapped polaron density, k_0 is the initial polaron recombination coefficient.

As mentioned above, an exact solution was employed to quantify polaron transient dynamics as below,

$$n(t) = \frac{N_0 k_T}{k - k_T}(exp(-k_T t) - exp(-kt))$$

1.8 Energetic Disorder Measurement

Energetic disorders of hole (σ_h) and electron (σ_e) were evaluated by performing temperature-dependent charge transport measurements. Herein, the Gaussian disorder model (GDM) is used to analyze the temperature-dependent hole and electron mobilities (μ_h and μ_e),[6, 7] that is,

$$\mu_0 = \mu_\infty exp\left[-\left(\frac{2\sigma}{3k_B T}\right)^2\right]$$

where μ_0 is the zero-field mobility, μ_∞ is the intercept from the plot of μ_0 *versus* $1/T^2$, k_B is the Boltzmann constant and T is the thermodynamic temperature.

In addition, the degree of the energetic disorders can be also quantified by an Urbach energy (E_U) according to the following Urbach's rule[8, 9]

$$\alpha(E) = \alpha_0 exp\left[\frac{E - E_g}{E_U}\right]$$

herein, $\alpha(E)$ is the absorption coefficient of the disordered semiconductors, α_0 is the optical absorption coefficient at the band edge, E is the photon energy. It should be noted that a smaller E_U demonstrates a lower degree of the energetic disorders.

1.9 Trap Density Measurement

Trap density, trap depth and the trap state gaussian width were estimated using capacitance-frequency measurements according to the following method.[10] Firstly, the frequency axis (f) was transformed into the energy axis (E_ω) as below,

$$E_\omega = kT ln\left(\frac{2v_0}{\omega}\right)$$

where ω is the angular frequency calculated from $\omega = 2\pi f$, v_0 is the attempt-to-escape frequency (10^9 Hz). Then, trap density (N_t) at energy E_ω was obtained from the derivative of the measured capacitance relative to the frequency described by

$$N_t(E_\omega) = -\frac{V_{bi} dC}{qL d\omega kT}\omega$$

where L is the thickness of the photoactive layer, V_{bi} is the built-in potential calculated from the Mott-Schottky plot ($1/C^2$ versus V) as below,

$$\frac{1}{C^2} = \frac{2(V_{bi} - V)}{q\varepsilon_0 \varepsilon N_{ap}}$$

where V is the applied bias voltage, N_{ap} is the doping parameter. Finally, the energy distribution of the density of states (DOS) was expressed by a Gaussian shape distribution given by

$$N_t(E) = \frac{N_t}{\sqrt{2\pi}\sigma} exp\left[-\frac{(E_t - E)^2}{2\sigma^2}\right]$$

where N_t is the total density (cm^{-3}), E_t is the center of the DOS, σ is the disorder parameter.

1.10 Energy Loss Measurement

The energy loss of OSCs was determined according to the following equation[11, 12] of

$$E_{loss} = E_g - qV_{OC} = \left(E_g - qV_{OC}^{rad}\right) + \left(qV_{OC}^{rad} - qV_{OC}\right)$$

where E_g is the band gap and V_{OC}^{rad} is the V_{OC} when only considering radiative recombination with realistic absorption edges. When all recombination is radiative, the related radiative limit V_{OC}^{rad} was calculated according to the following equation given by

$$V_{OC}^{rad} = \frac{kT}{q} ln\left(\frac{J_{SC}}{J_0^{rad}} + 1\right) = \frac{kT}{q} ln(\frac{q\int_0^\infty EQE_{PV}(E) \cdot \emptyset_{AM1.5}(E)dE}{q\int_0^\infty EQE_{PV}(E) \cdot \emptyset_{BB}(E)dE} + 1)$$

herein, J_0^{rad} is the saturated current density for radiative recombination, $\Phi_{BB}(E)$ is the blackbody spectrum with the following expression as below,

$$\phi_{BB}(E) = \frac{2\pi E^2}{h^3 c^2} exp(-\frac{E}{kT})$$

where h is the Planck's constant and c is the light speed in a vacuum. Moreover, the nonradiative voltage loss (V_{OC}^{nonrad}) was quantified through[11, 12]

$$V_{OC}^{nonrad} = V_{OC}^{rad} - V_{OC}$$

As for the band gap of the actual OPV devices (E_g^{PV}), it was obtained from the FTPS-EQE spectrum described by[13]

$$E_g^{PV} = \frac{\int_a^b E \cdot P(E) \cdot dE}{\int_a^b P(E) \cdot dE}$$

where $P(E)$ is the distribution of the calculated band gap ($P(E) = dEQE/dE$). Especially, the integral boundaries (a, b) were selected where $P(a) = P(b) = 0.5max[P(E)]$.

2. Supplementary Figures

(a)

(b)

(c)
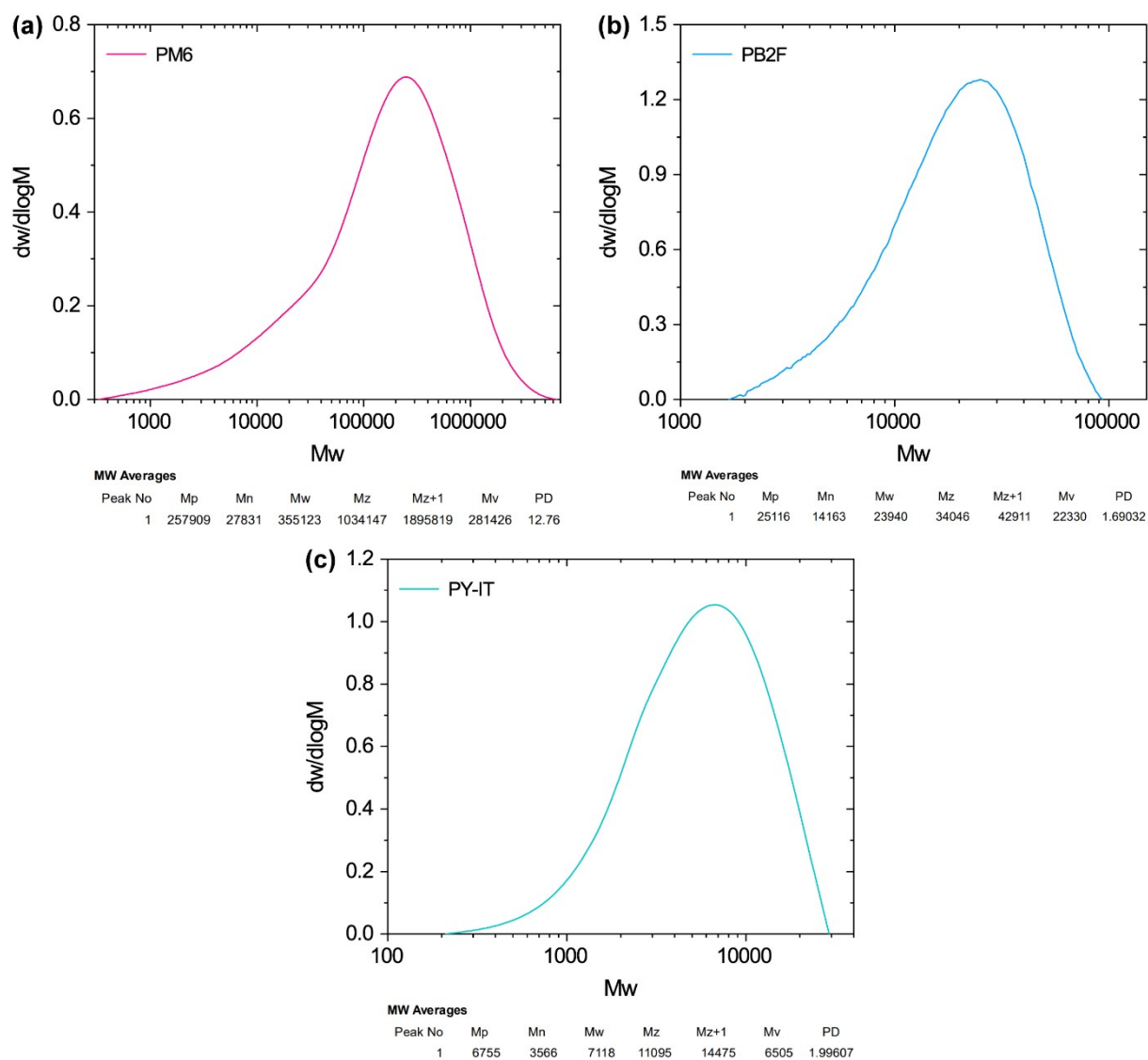
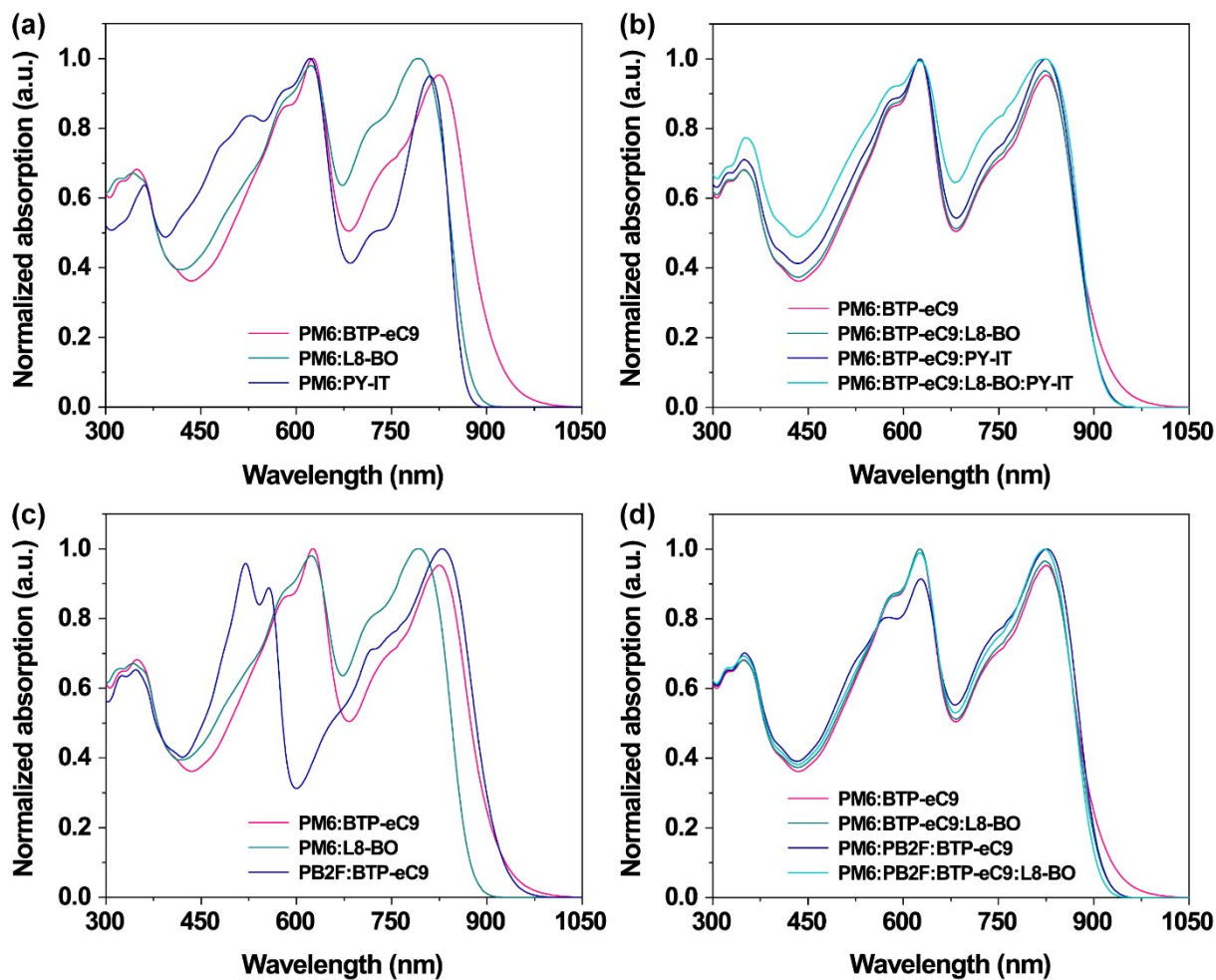**Fig. S1** Gel permeation chromatography (GPC) curves of (a) PM6, (b) PB2F and (c) PY-IT.

Fig. S2 (a-d) Normalized UV-vis absorption spectra of PM6:BTP-eC9-based binary, ternary and quaternary blend films processed by chloroform.
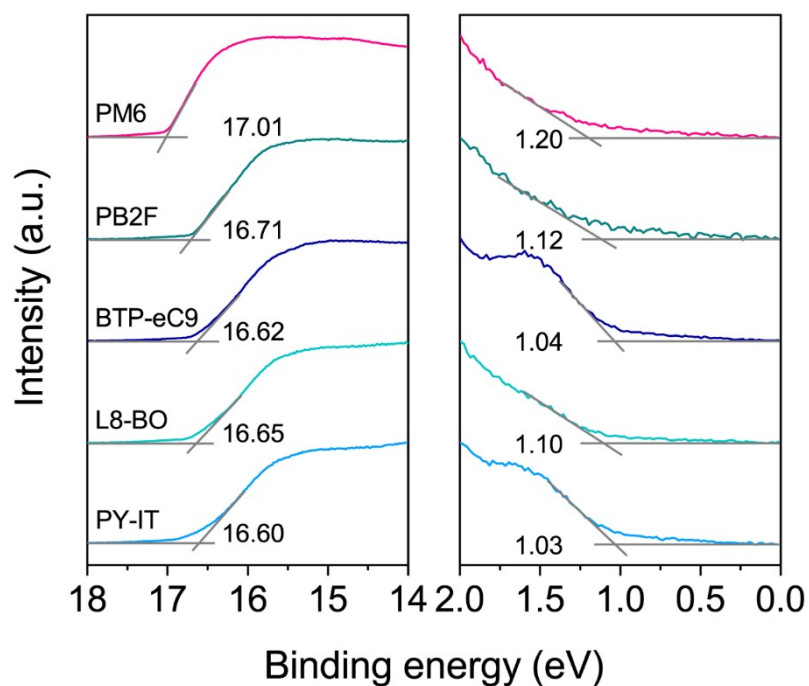
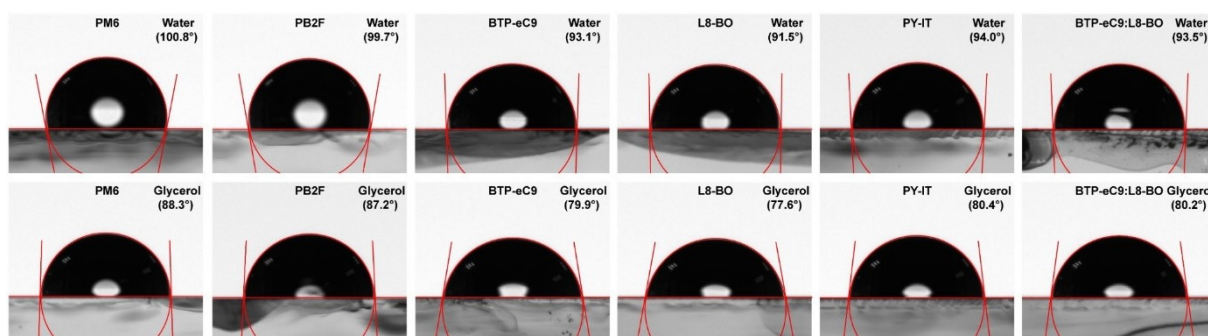**Fig. S3** Ultraviolet photoelectron spectroscopy (UPS) spectra of PM6, PB2F, BTP-eC9, L8-BO and PY-IT neat films.

Fig. S4 Contact angle images of PM6, PB2F, BTP-eC9, L8-BO, PY-IT and BTP-eC9:L8-BO films with water and glycerol droplet on top.
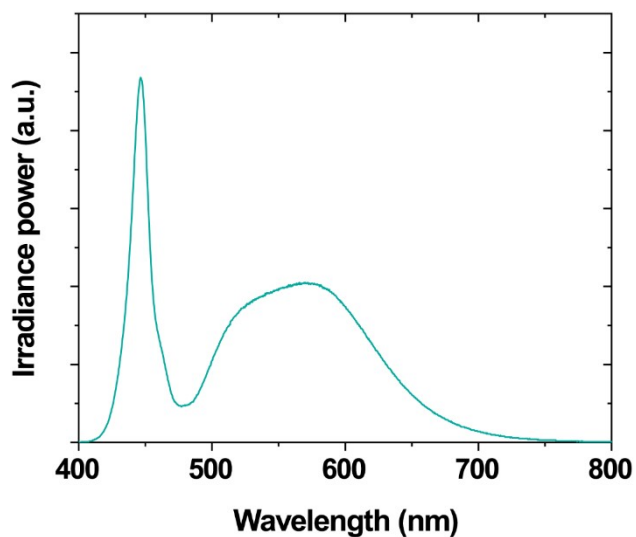
Fig. S5 Light spectrum of the white LED used for photothermal stability test in this work.
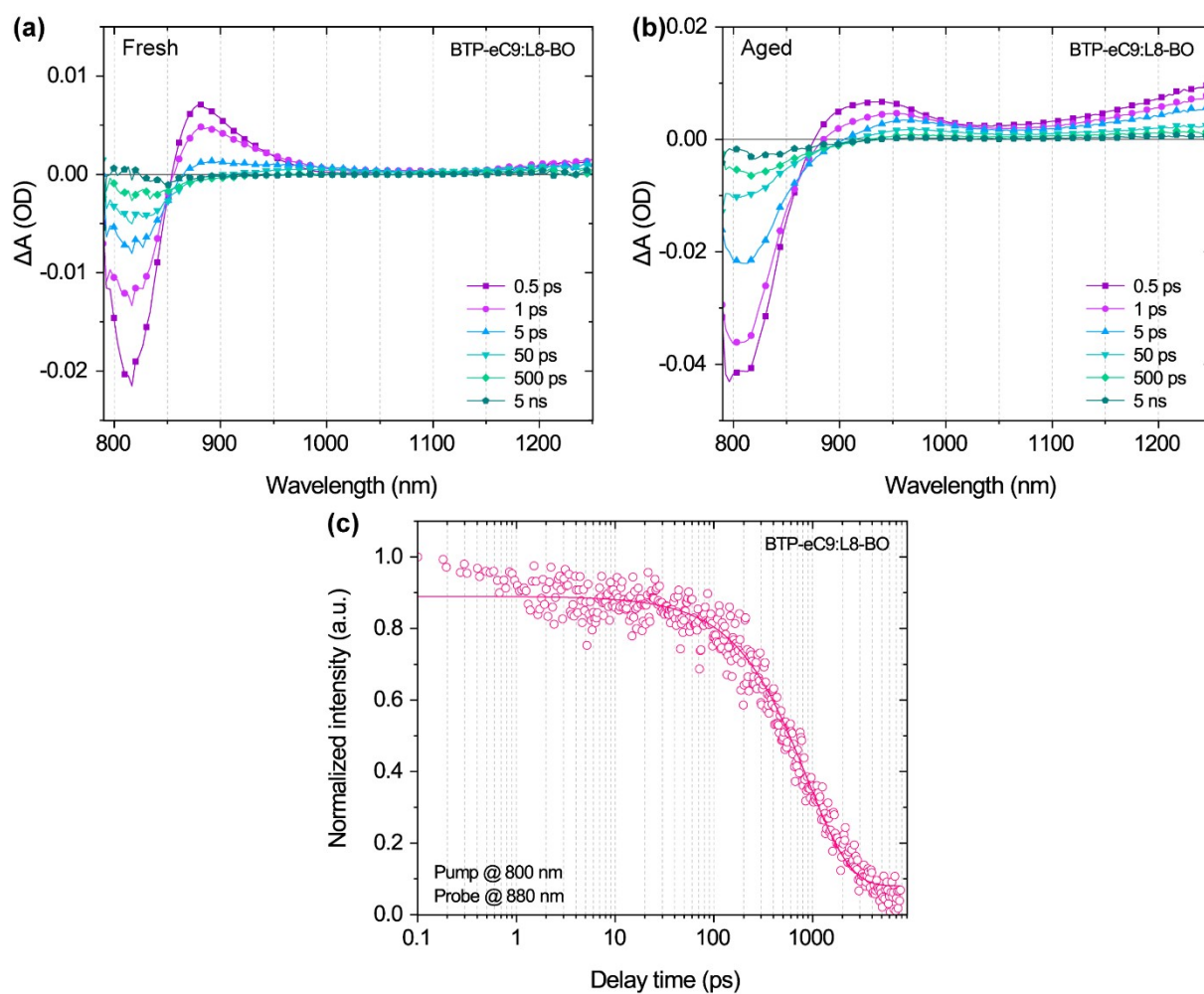

Fig. S6 TA spectra of BTP-eC9:L8-BO blend film (a) before and (b) after photothermal aging for 200 h. (c) Exciton decay trace of BTP-eC9:L8-BO blend film under 800 nm excitation with a very low excitation fluence (1 μJ cm^{-2}).
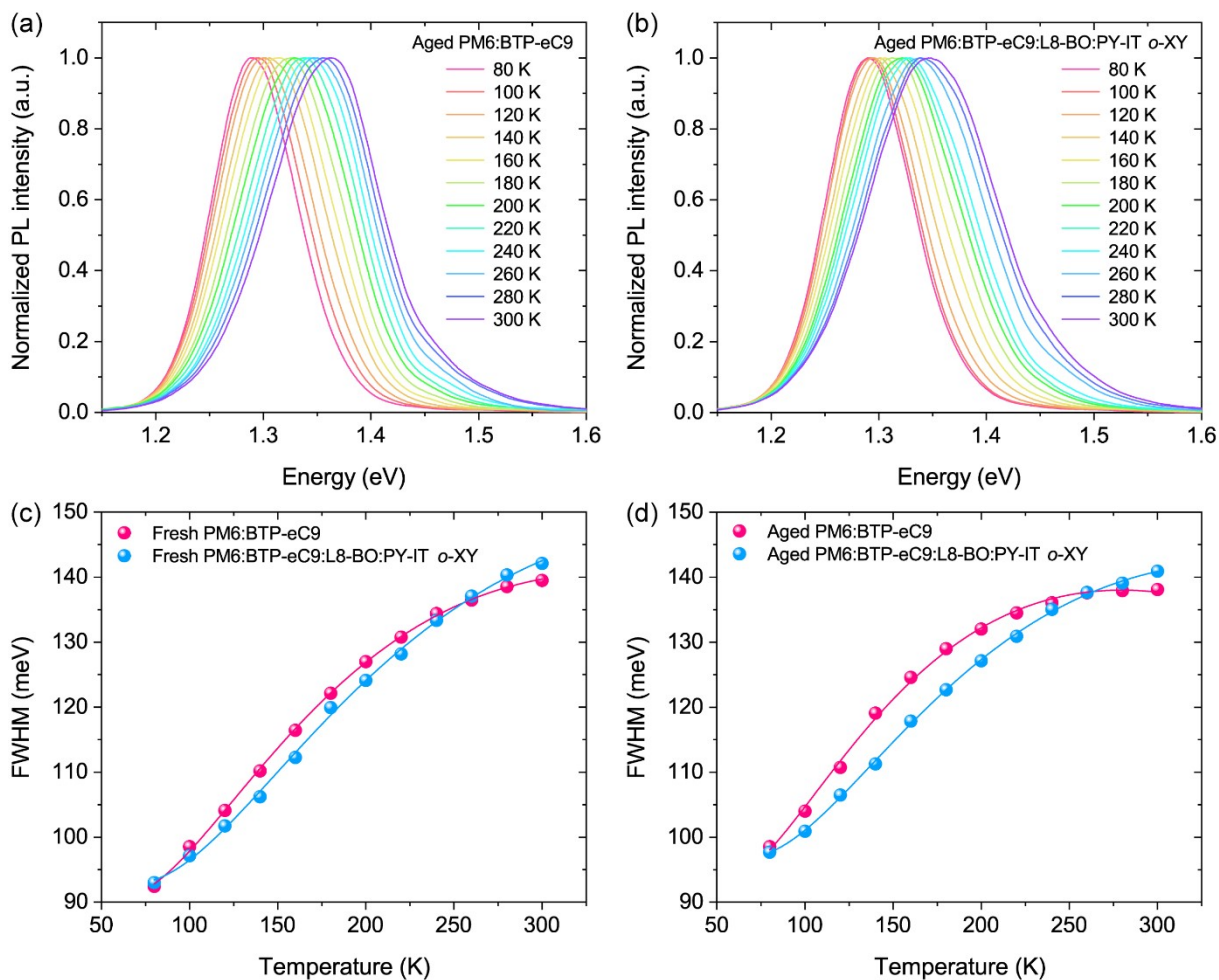
Fig. S7 Normalized temperature-dependent PL spectra of the aged (a) PM6:BTP-eC9 binary blend film processed by chloroform and (b) PM6:BTP-eC9:L8-BO:PY-IT quaternary blend film processed by *o*-xylene for 200 h. The corresponding PL linewidths of the (c) fresh and (d) aged binary blend films processed by chloroform and quaternary blend films processed by *o*-xylene.
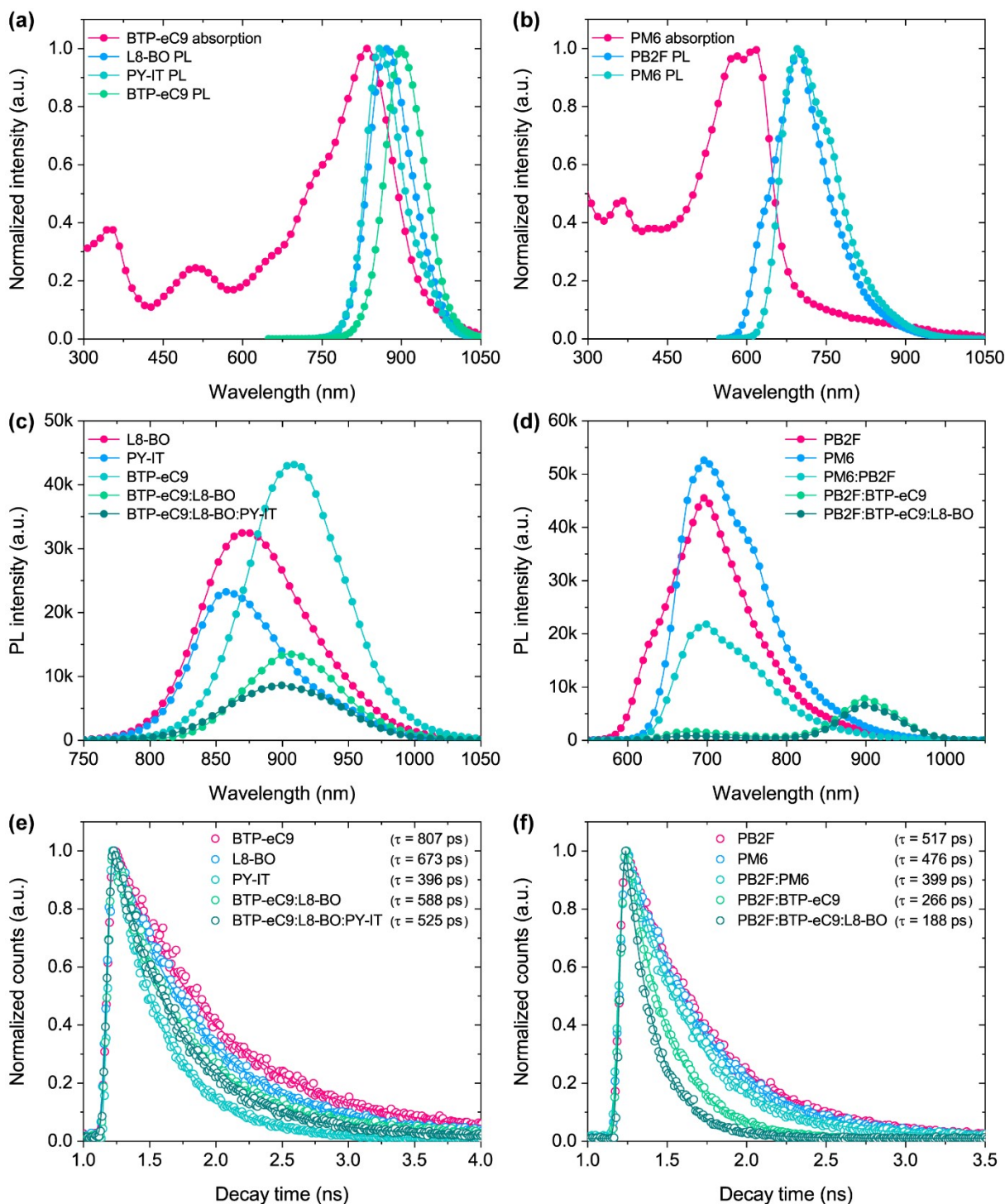
Fig. S8 Normalized absorption and PL spectra of (a) L8-BO, PY-IT and BTP-eC9 films and (b) PM6 and PB2F films. PL spectra of (c) L8-BO, PY-IT, BTP-eC9, BTP-eC9:L8-BO and BTP-eC9:L8-BO:PY-IT films and (d) PB2F, PM6, PM6:PB2F, PB2F:BTP-eC9 and PB2F:BTP-eC9:L8-BO films. Normalized TRPL spectra of (e) L8-BO, PY-IT, BTP-eC9, BTP-eC9:L8-BO and BTP-eC9:L8-BO:PY-IT films and (f) PB2F, PM6, PB2F:PM6, PB2F:BTP-eC9 and PB2F:BTP-eC9:L8-BO films.
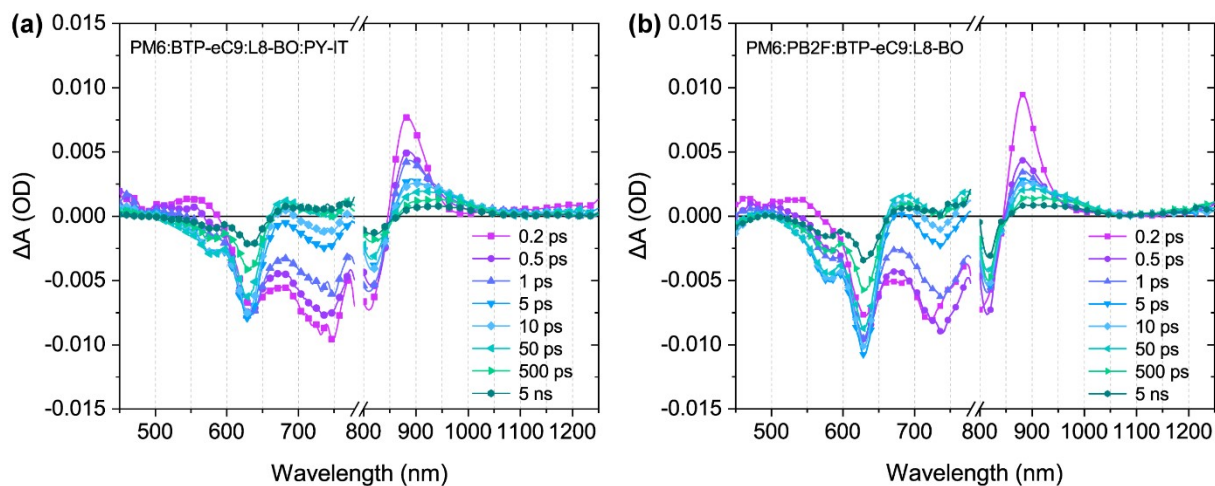
Fig. S9 TA spectra of (a) PM6:BTP-eC9:L8-BO:PY-IT and (b) PM6:PB2F:BTP-eC9:L8-BO quaternary blend films processed by chloroform.
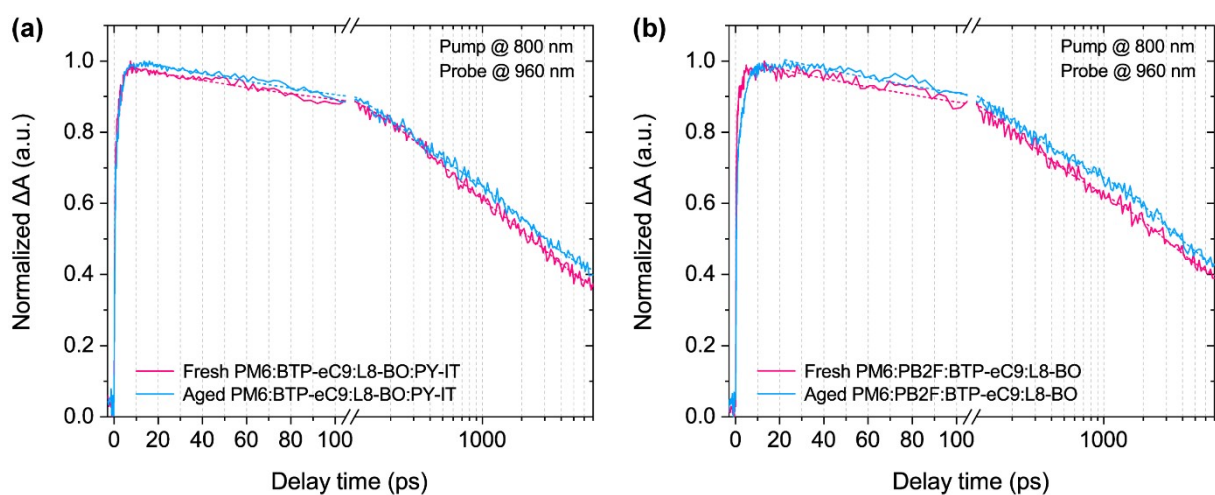

Fig. S10 Normalized kinetic traces probed at 960 nm and the corresponding fitting curves for (a) PM6:BTP-eC9:L8-BO:PY-IT and (b) PM6:PB2F:BTP-eC9:L8-BO quaternary blend films processed by chloroform before and after continuous photothermal aging for 200 h.

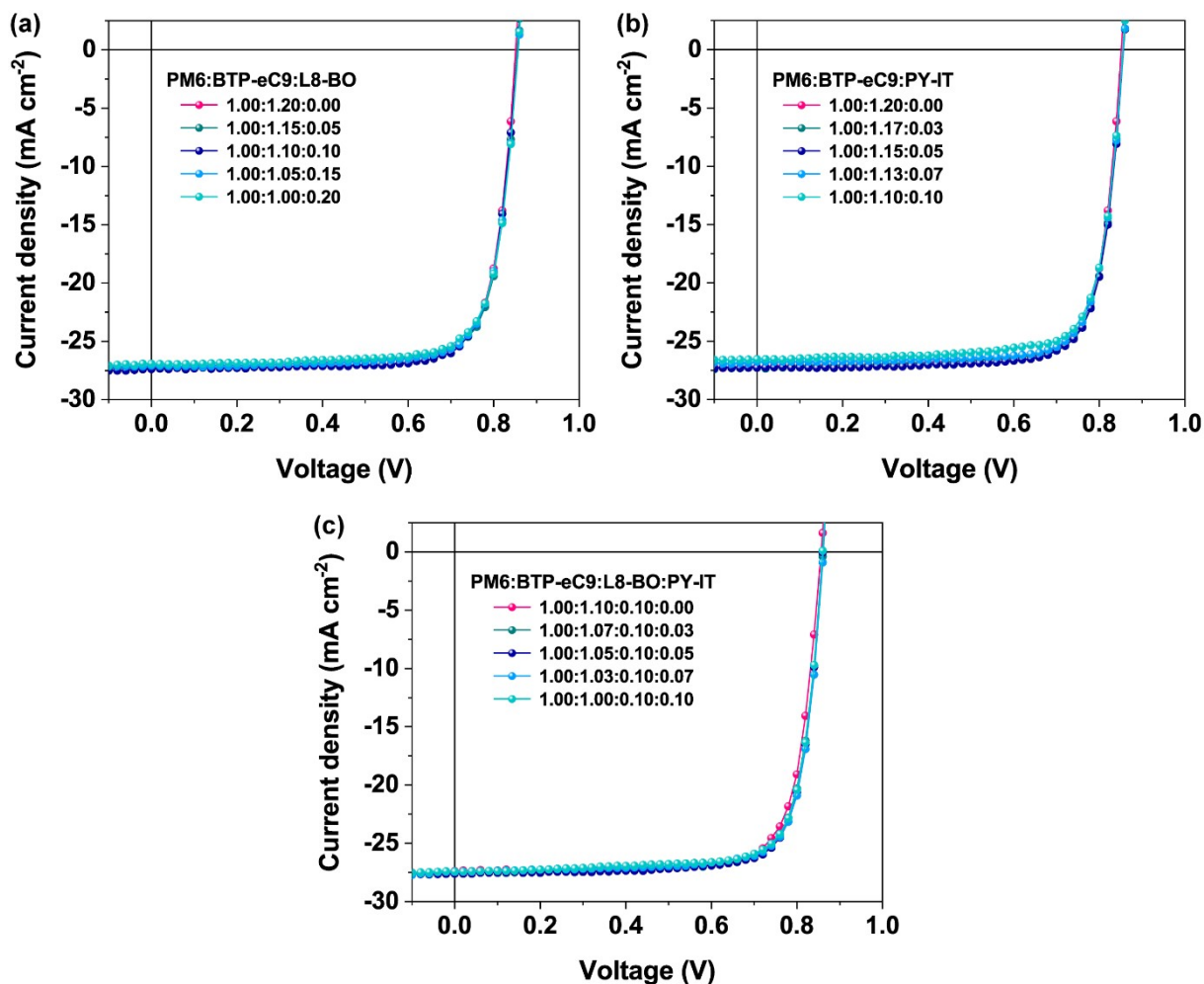**Fig. S11** *J-V* curves of (a) PM6:BTP-eC9-based ternary OSCs with various L8-BO content, (b) PM6:BTP-eC9-based ternary OSCs with various PY-IT content and (c) PM6:BTP-eC9:L8-BO-based quaternary OSCs with various PY-IT content.
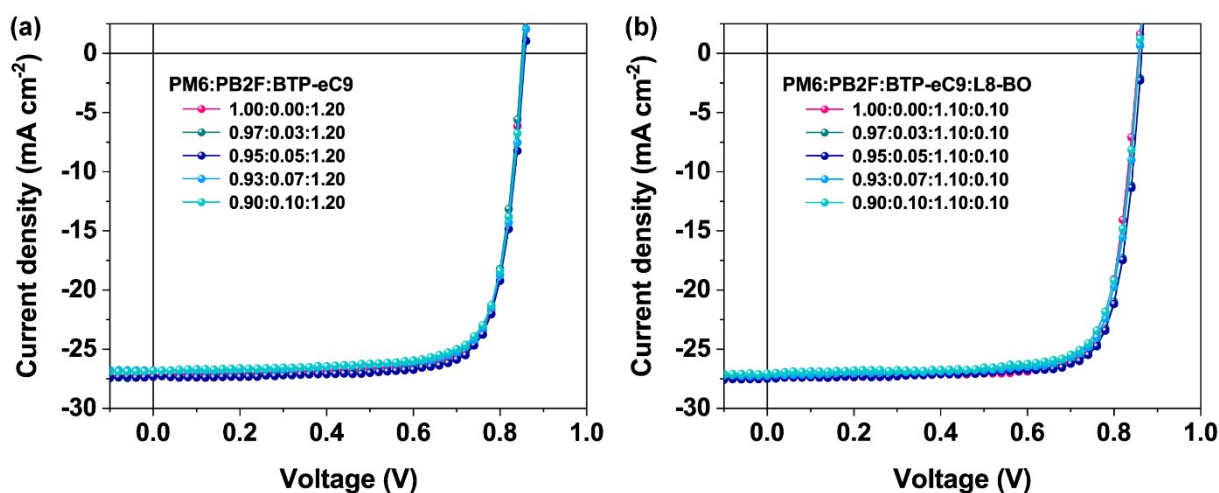
Fig. S12 *J-V* curves of (a) PM6:BTP-eC9-based ternary OSCs with various PB2F content and (b) PM6:BTP-eC9:L8-BO-based quaternary OSCs with various PB2F content.
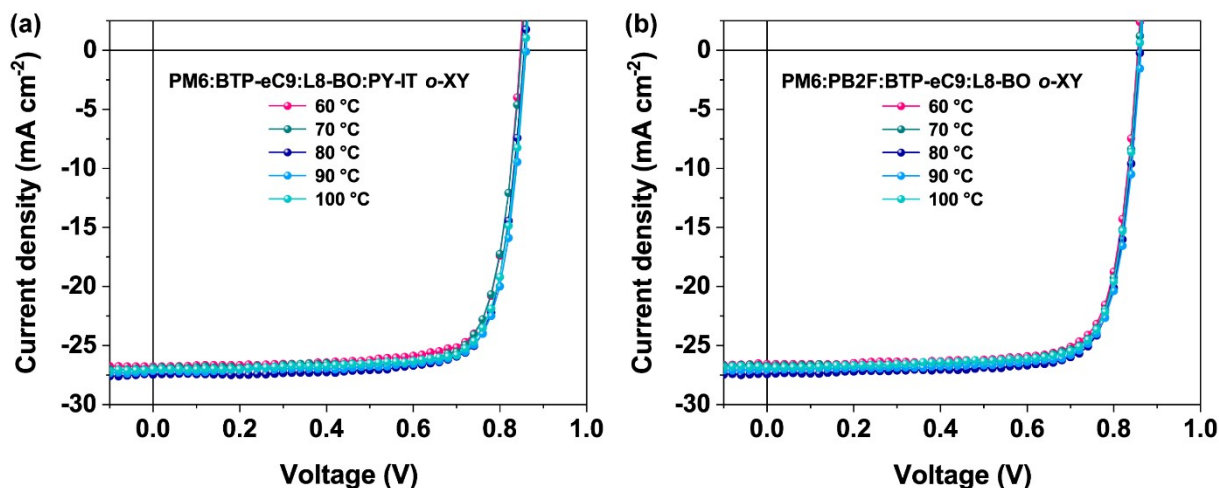
Fig. S13 *J-V* curves of (a) PM6:BTP-eC9:L8-BO:PY-IT and (b) PM6:PB2F:BTP-eC9:L8-BO quaternary OSCs processed by *o*-xylene with hot-spin coating at various temperatures.
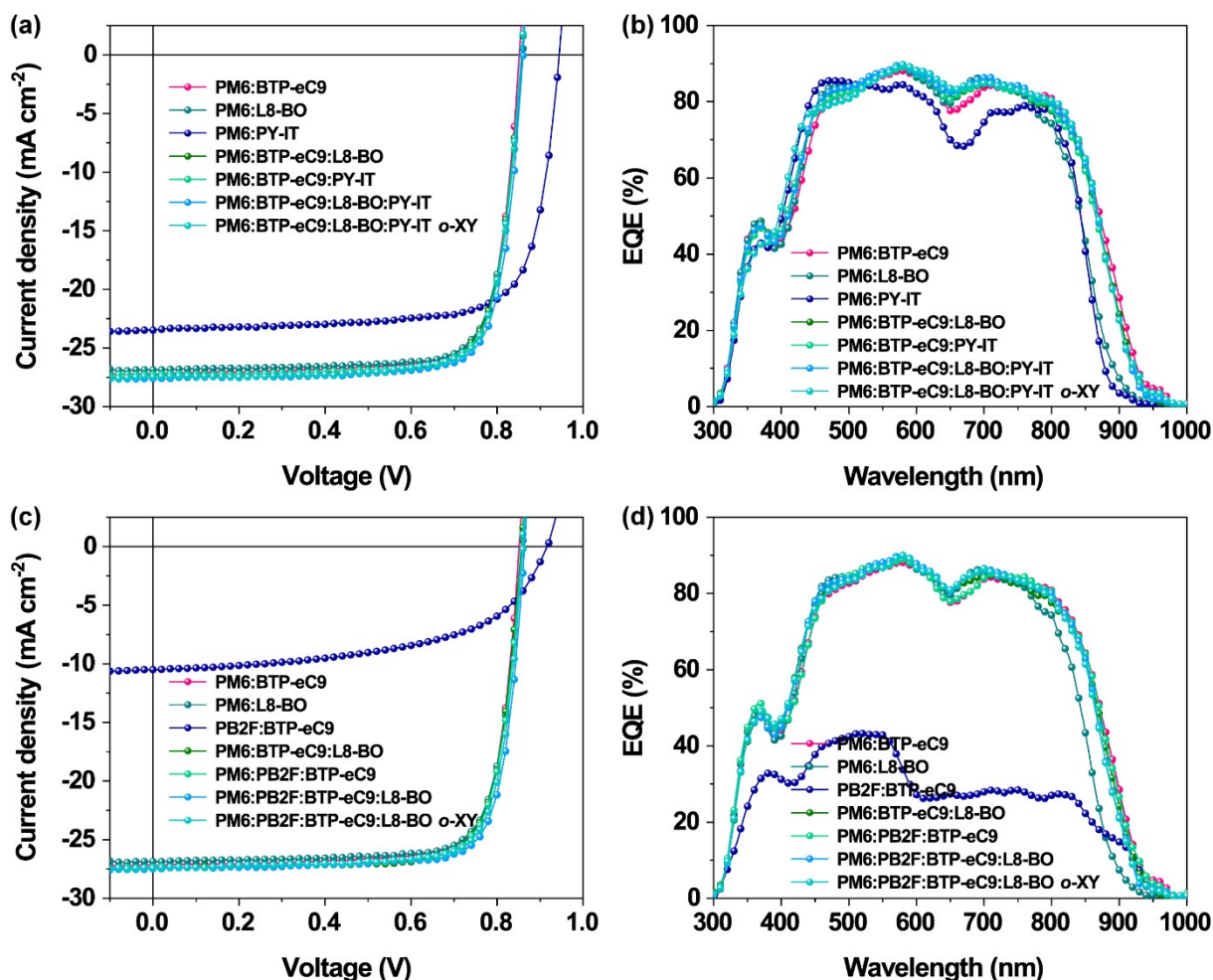
Fig. S14 (a) *J-V* curves and (b) EQE spectra of various binary, ternary and quaternary OSCs based on PM6:BTP-eC9:L8-BO:PY-IT system. (c) *J-V* curves and (d) EQE spectra of various binary, ternary and quaternary OSCs based on PM6:PB2F:BTP-eC9:L8-BO system.
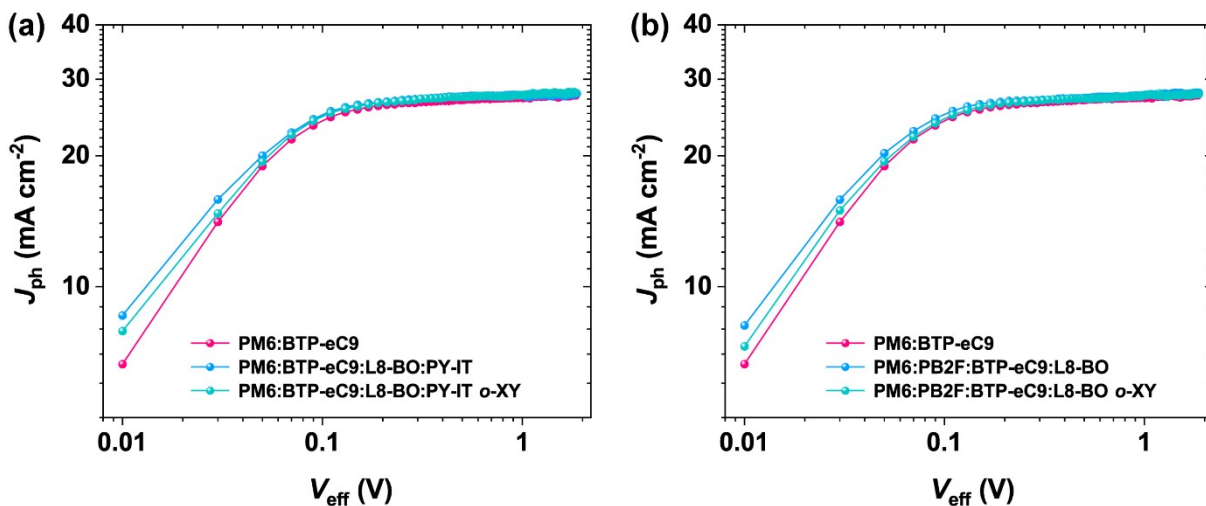
Fig. S15 (a) J_{ph}-V_{eff} curves of PM6:BTP-eC9:L8-BO:PY-IT-based binary and quaternary OSCs with different solvent treatments. (b) J_{ph}-V_{eff} curves of PM6:PB2F:BTP-eC9:L8-BO-based binary and quaternary OSCs with different solvent treatments.
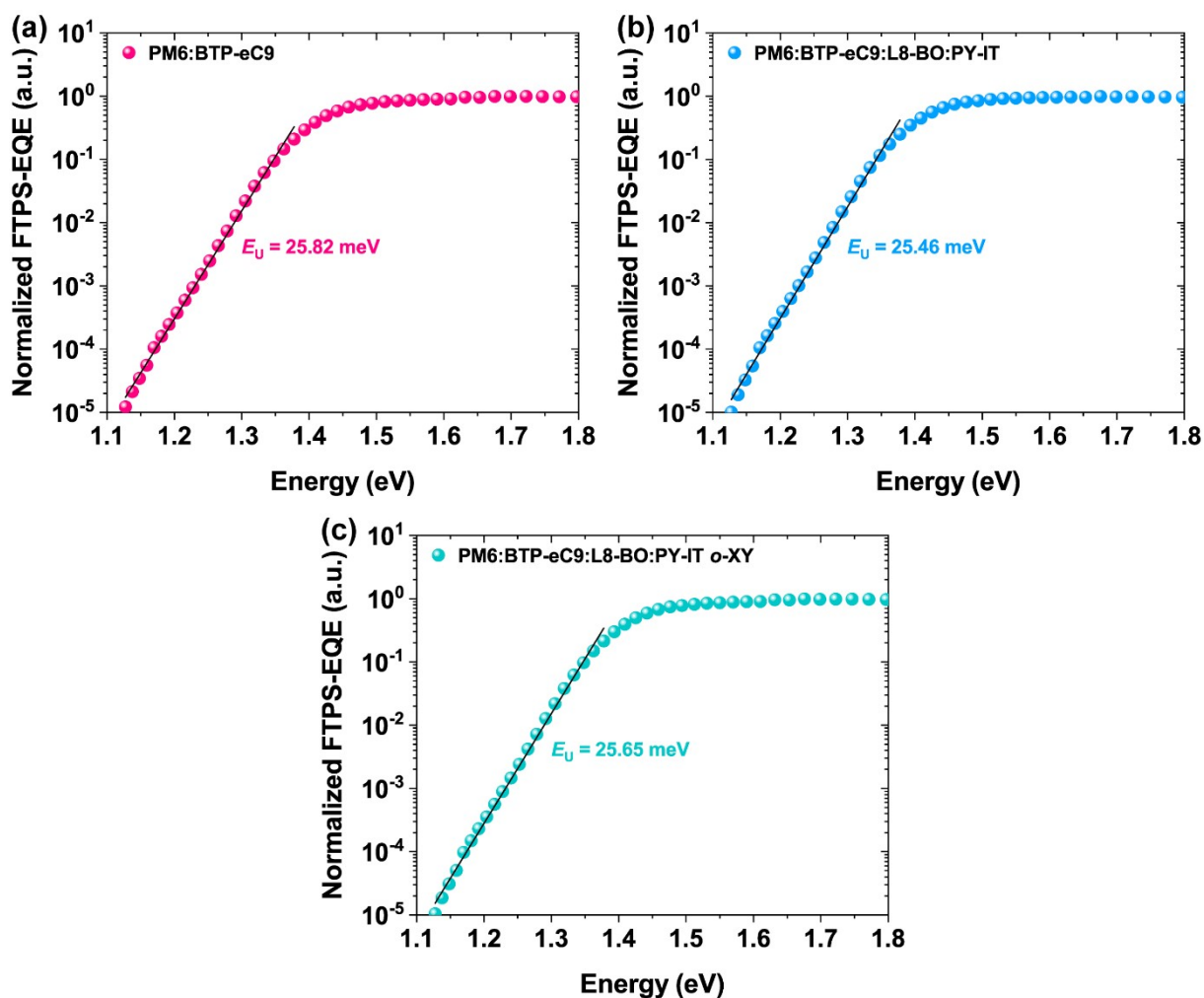
Fig. S16 (a-c) Normalized FTPS-EQE spectra of PM6:BTP-eC9:L8-BO:PY-IT-based binary and quaternary OSCs with different solvent treatments at absorption onset.
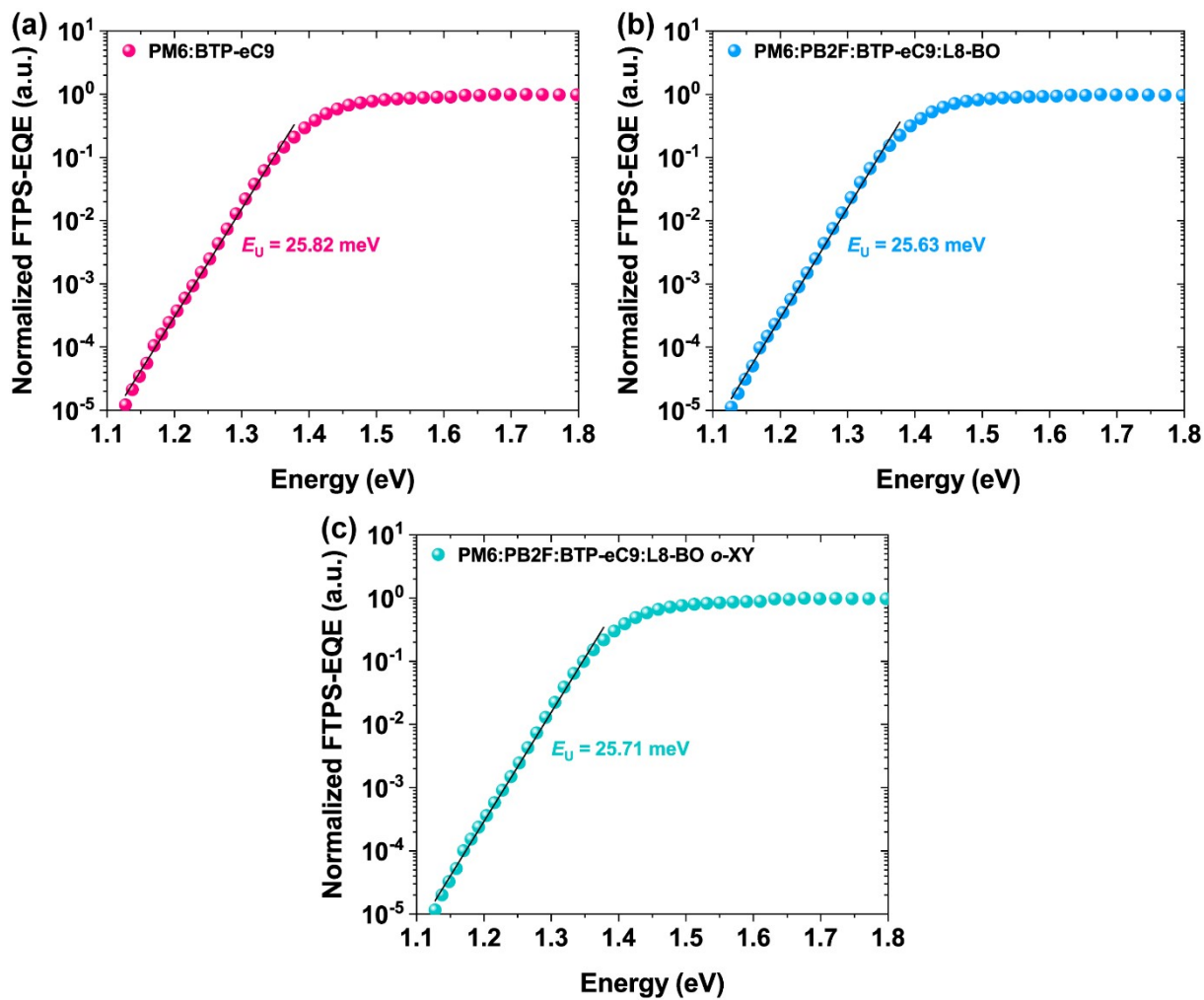
Fig. S17 (a-c) Normalized FTPS-EQE spectra of PM6:PB2F:BTP-eC9:L8-BO-based binary and quaternary OSCs with different solvent treatments at absorption onset.
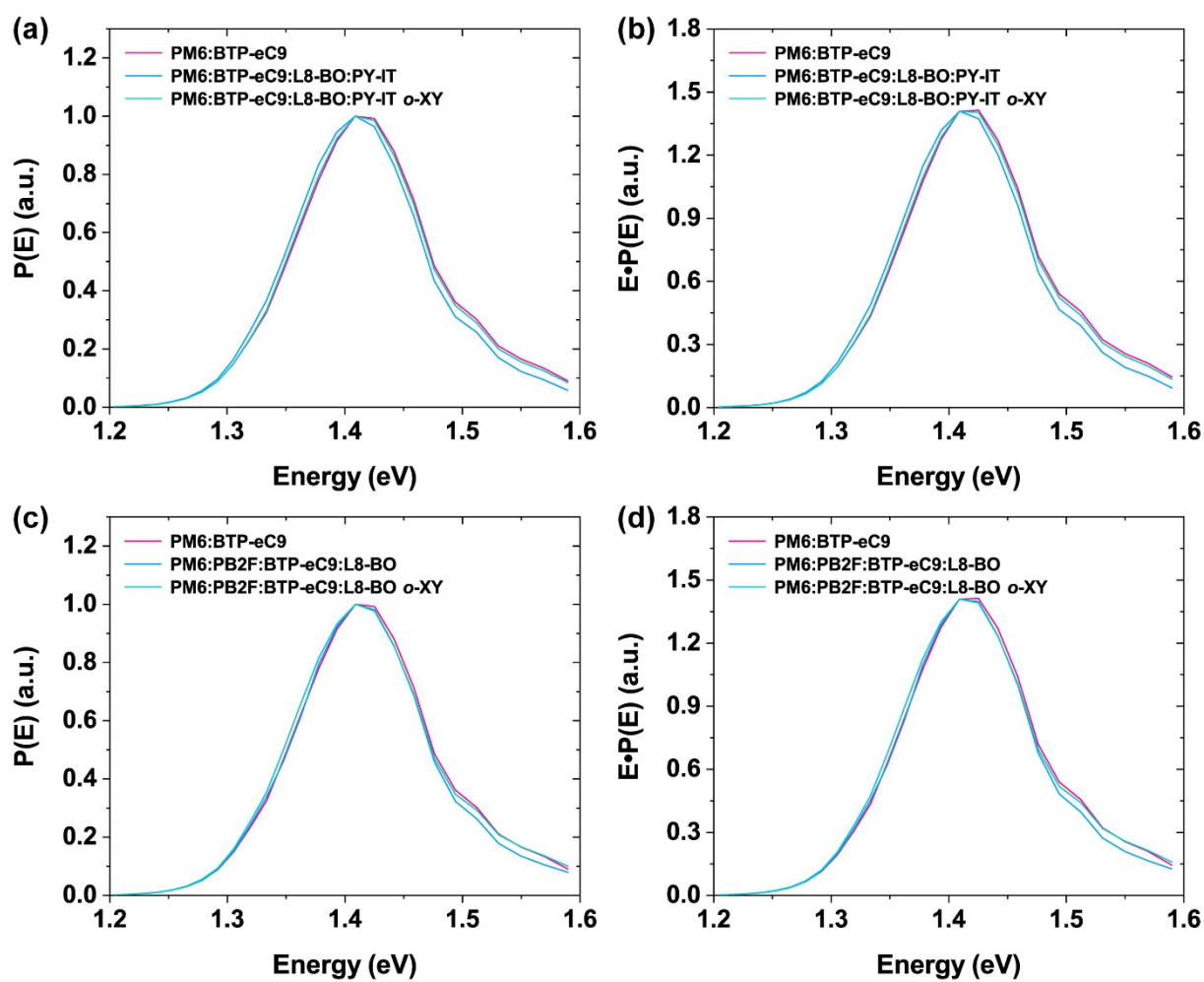
Fig. S18 Bandgap distribution obtained from FTPS-EQE spectra for (a,b) PM6:BTP-eC9:L8-BO:PY-IT and (c,d) PM6:PB2F:BTP-eC9:L8-BO-based binary and quaternary OSCs with different solvent treatments.
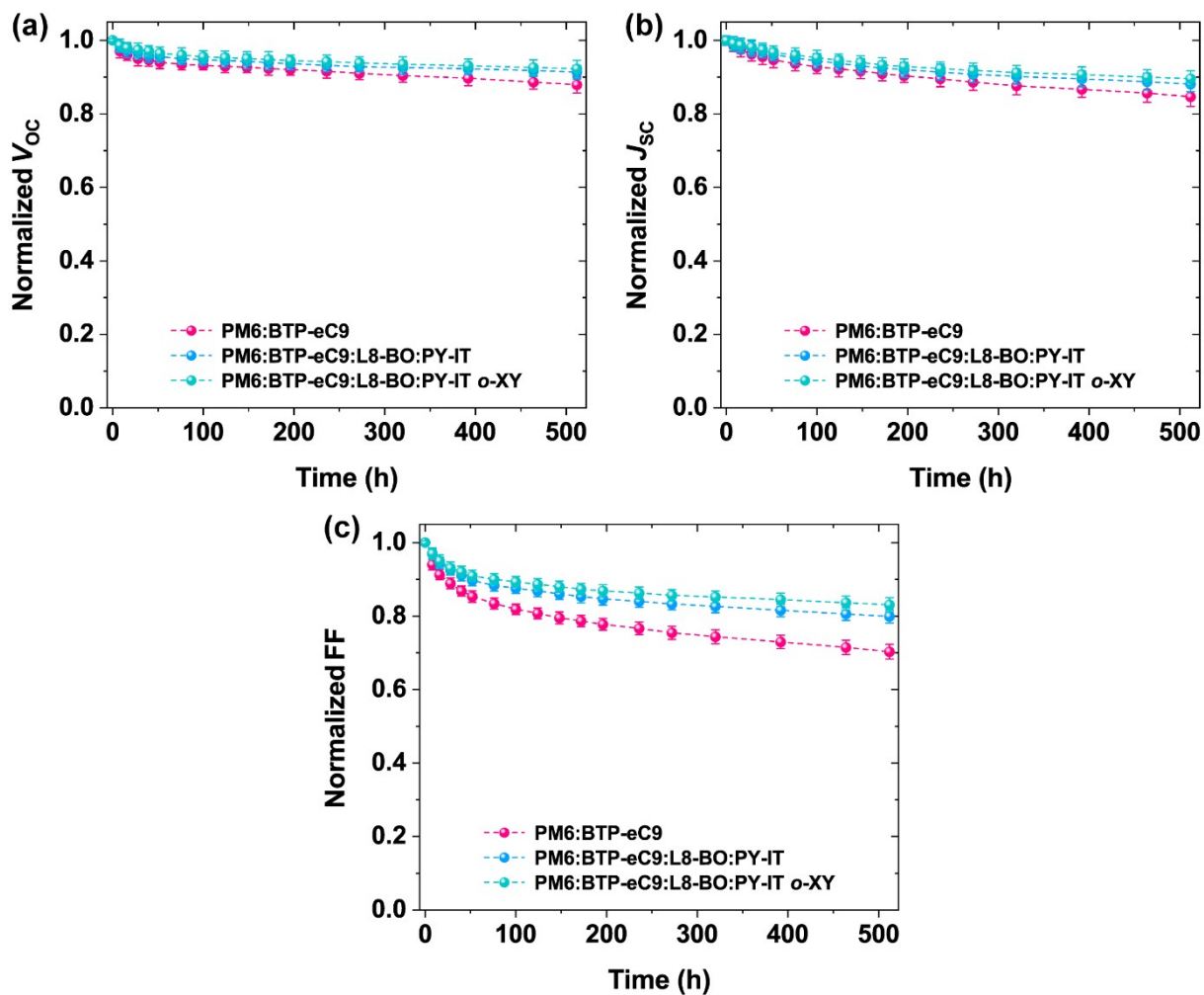
Fig. S19 Normalized (a) V_{OC}, (b) J_{SC} and (c) FF decay traces of PM6:BTP-eC9:L8-BO:PY-IT-based binary and quaternary OSCs with different solvent treatments under the illumination of a 100 mW cm^{-2} white LED at 50-55 °C.
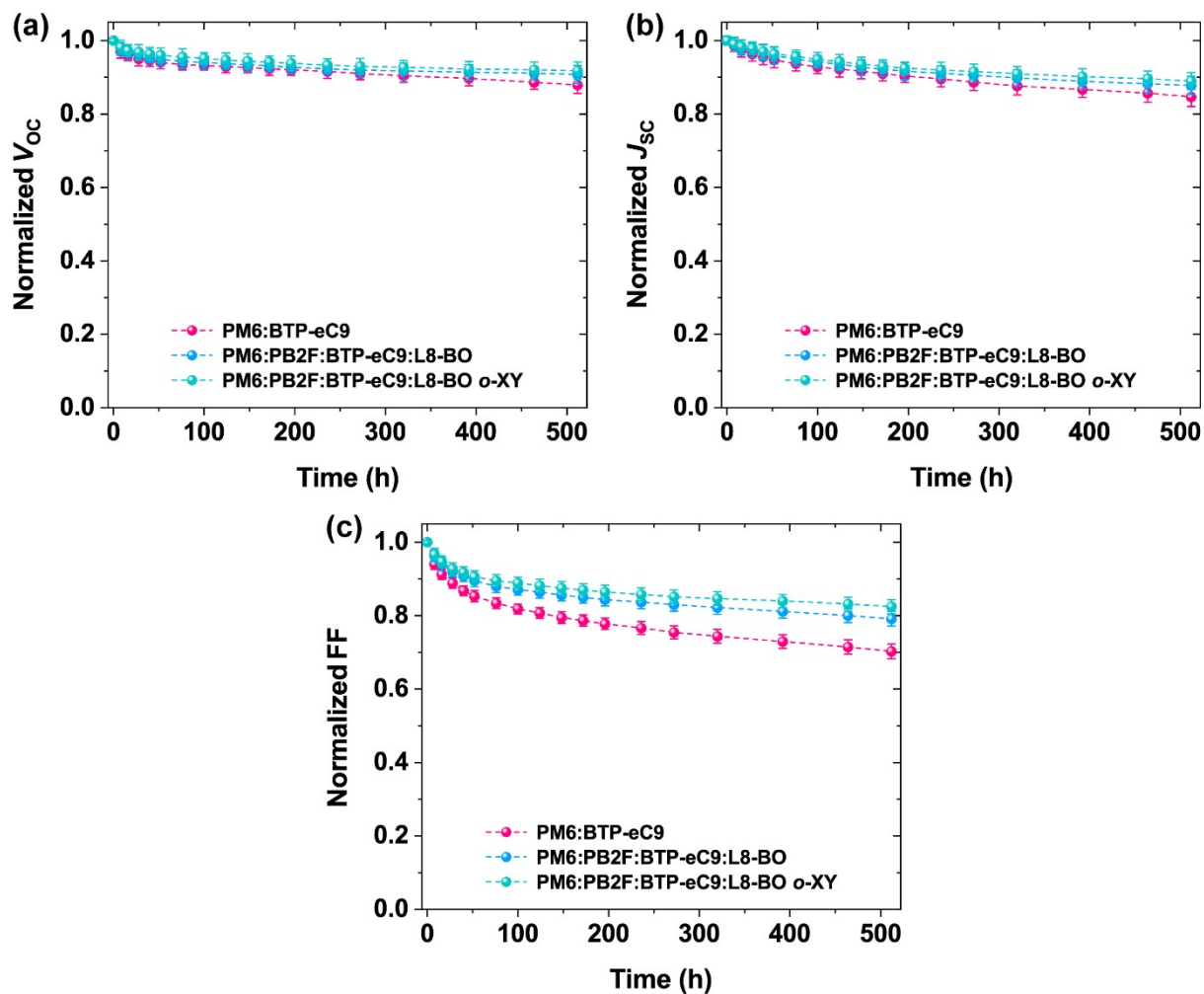
Fig. S20 Normalized (a) V_{OC}, (b) J_{SC} and (c) FF decay traces of PM6:PB2F:BTP-eC9:L8-BO-based binary and quaternary OSCs with different solvent treatments under the illumination of a 100 mW cm^{-2} white LED at 50-55 °C.
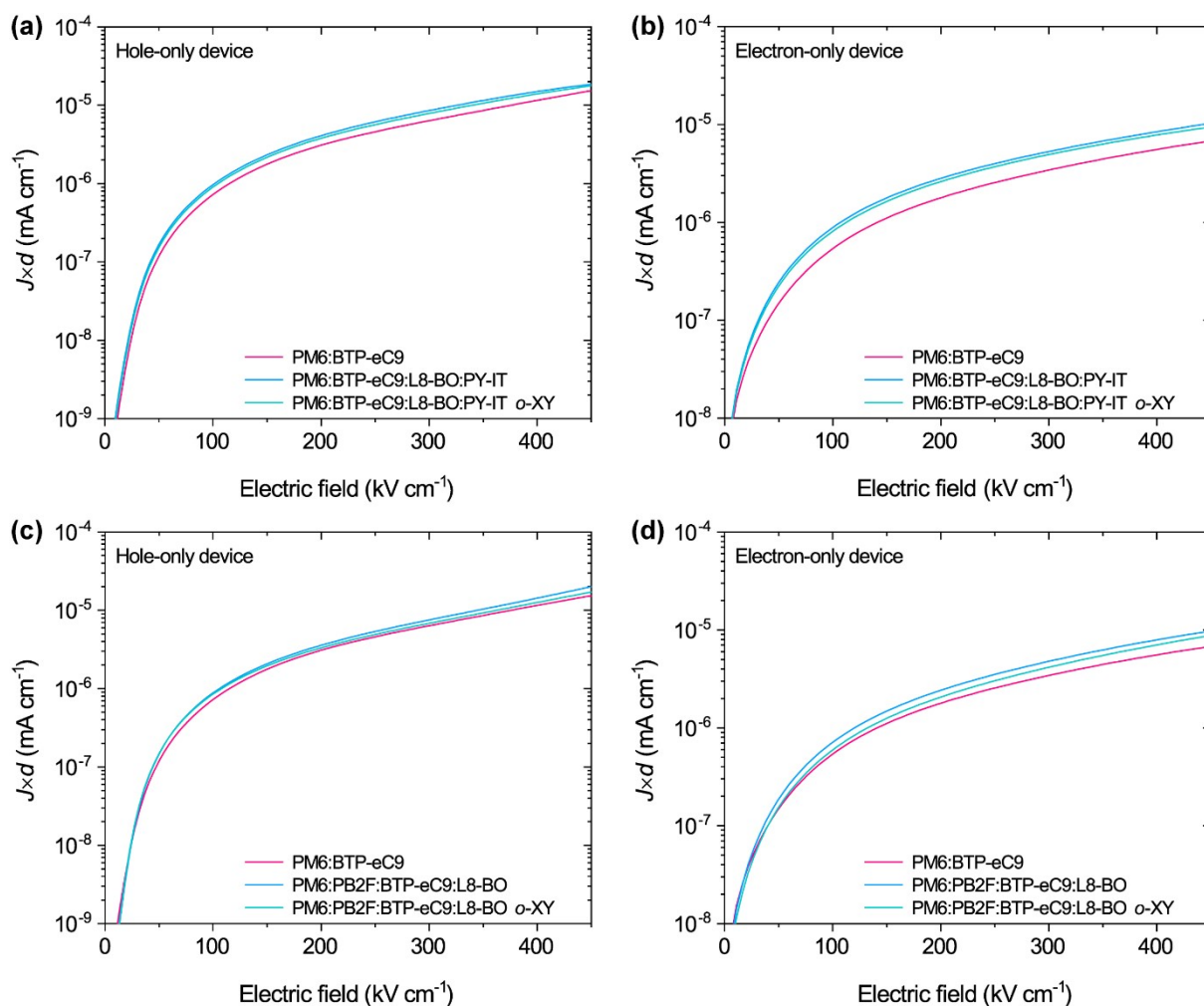
Fig. S21 The dark *J-V* curves of PM6:BTP-eC9:L8-BO:PY-IT-based binary and quaternary (a) hole-only and (b) electron-only devices with different solvent treatments. The dark *J-V* curves of PM6:PB2F:BTP-eC9:L8-BO-based binary and quaternary (c) hole-only and (d) electron-only devices with different solvent treatments.
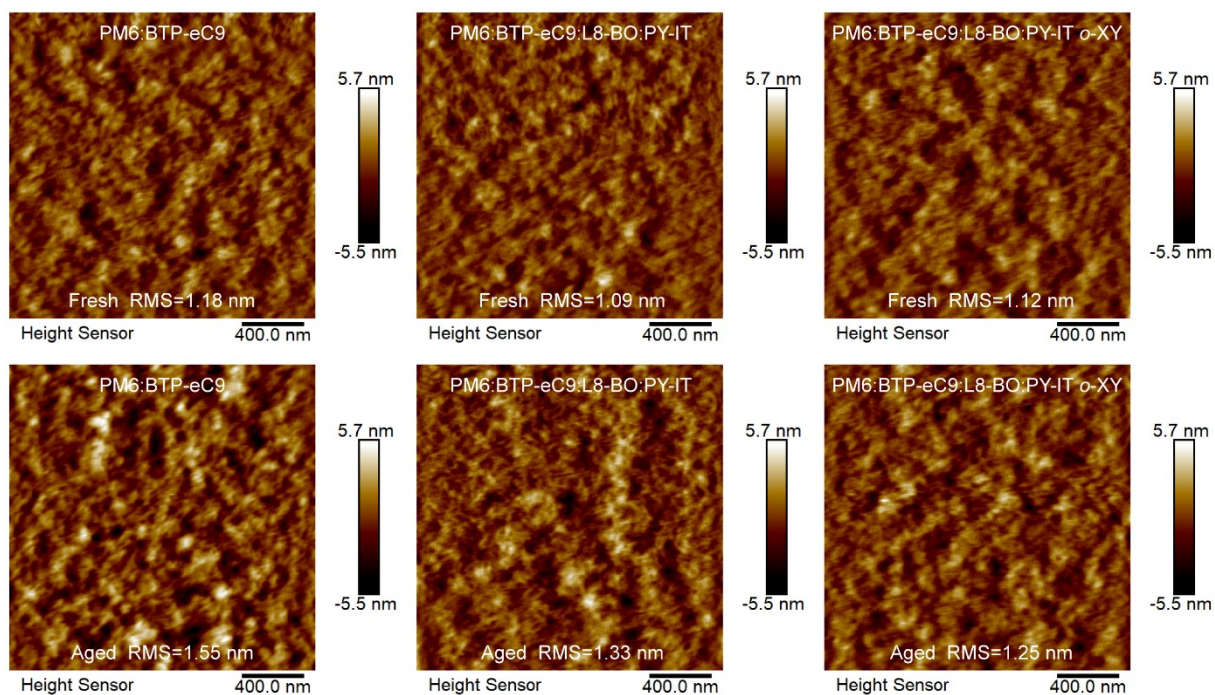
Fig. S22 AFM height images of PM6:BTP-eC9:L8-BO:PY-IT-based binary and quaternary blend films with different solvent treatments before and after continuous photothermal aging for 200 h.
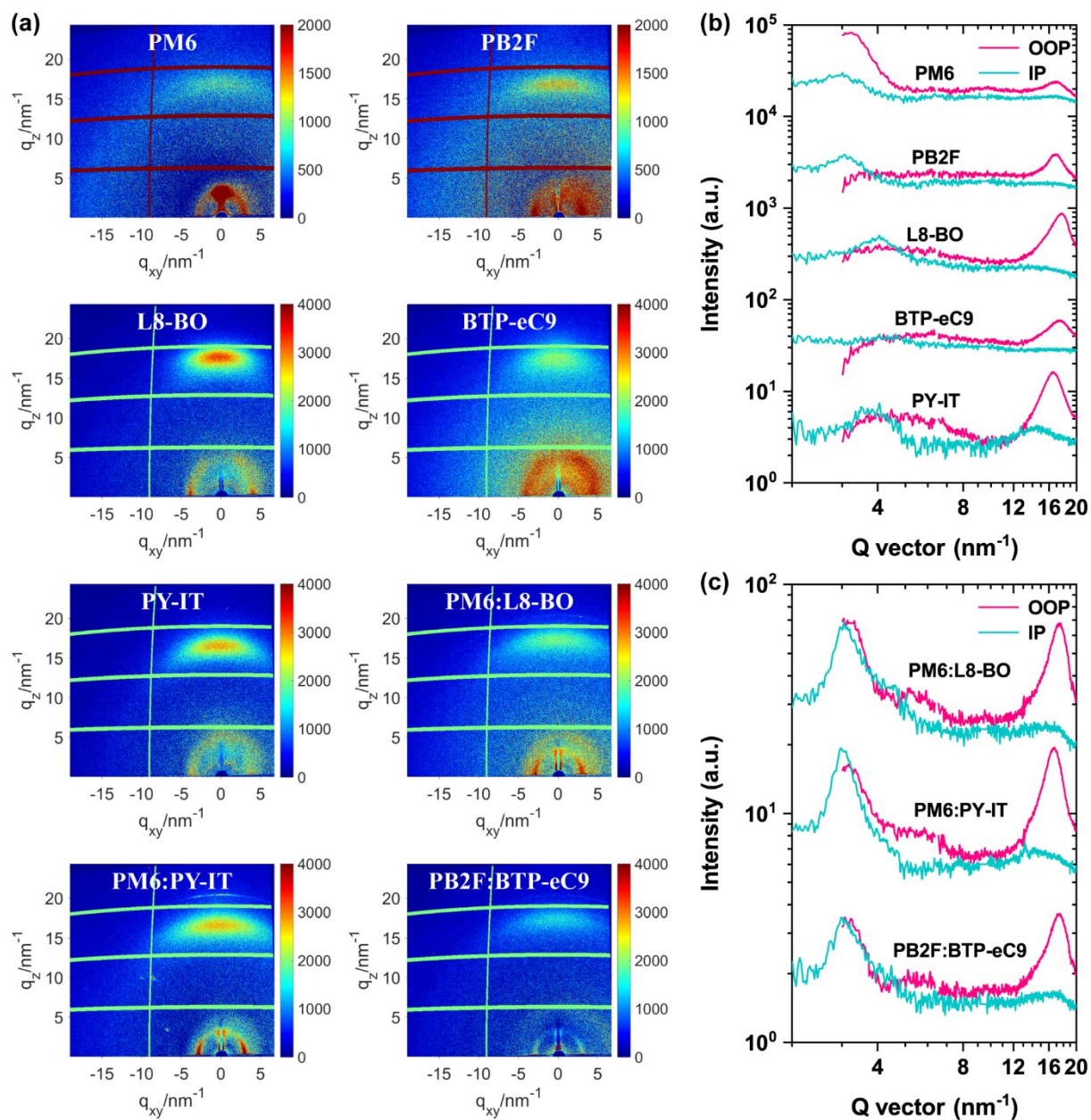
Fig. S23 (a) 2D GIWAXS patterns and the corresponding out-of-plane (OOP) and in-plane (IP) scattering profiles of (b) neat films and (c) binary blend films.

3. Supplementary Tables

Table S1. The recent progress made in revealing degradation mechanism and improving device lifetime of the state-of-the-art OSCs under various aging conditions.

Photoactive layer	Device structure	Aging condition	Degradation mechanism	Aging time (h)	Best PCE (%)	Retain (%)
PBDB-T:OY1[14]	Inverted	1 sun, N$_2$	Aggregation of OY1	200	14.20	84
PBDB-T:OY3[14]	Inverted	1 sun, N$_2$	Unclear	200	15.05	94
PBDB-T:POY[14]	Inverted	1 sun, N$_2$	Burn-in degradation	200	14.12	87
PM6:DY2[15]	Conventional	Maximum power point (MPP), 1 sun	Thermodynamic relaxation in mixed domains	700	17.85	83
PM6:DY2[15]	Conventional	100 ℃, N$_2$	Thermodynamic relaxation in mixed domains	480	17.85	100
PTzBI-dF:L8BO:Y6[16]	Inverted	85 ℃, N$_2$	Unstable amorphous phases in blends	1400	18.26	95
PM6:L15:PM6-b-L15[17]	Conventional	RT, N$_2$	Burn-in degradation	1000	11.78	90
PM6:L15:PM6-b-L15[17]	Conventional	1 sun	Aggregation	1000	11.78	83
PM6:L15:PM6-b-L15[17]	Conventional	85 ℃, N$_2$	Aggregation	1000	11.78	80
PM6:BTP-S11:BTP-S12[18]	Conventional	MPP, 1 sun	Burn-in degradation	1000	19.1	65
PM6:PY-DT+Y6[19]	Conventional	MPP, 1 sun	Degradation of molecules in blends	1180	18.02	80
D18:3-ClTh:BTP-Th[20]	Conventional	MPP, 1 sun	Degradation of vertical morphology	400	19.15	85
D18:3-ClTh:BTP-Th[20]	Conventional	65 ℃, N$_2$	Degradation of vertical morphology	1000	19.15	81
D18:3-ClTh[21]	Inverted	MPP, 1 sun, 65 ℃	Burn-in degradation	400	18.8	72
PM6:PY-1S1Se:PY-2Cl[22]	Conventional	MPP, 1 sun	Burn-in degradation	3000	18.2	77.5
PM6:Y6[23]	Inverted	1 sun, air	Twisting in the benzo[1,2-b:4,5-b0]dithiophene (BDT)-thiophene motif of PM6	12	14.87	14
D18:Y6[23]	Inverted	1 sun, air	Twisting in the benzo[1,2-b:4,5-b0]dithiophene (BDT)-thiophene motif of D18	12	15.11	52

Table S2. Key parameters of contact angle measurements by using water and glycerol droplets.

Film surface	θ_{water} (°)	$\theta_{glycerol}$ (°)	γ^d (mN m^{-1})	γ^p (mN m^{-1})	γ (mN m^{-1})	χ PM6	χ BTP-eC9
PM6	100.8	88.3	30.03	0.28	30.31	/	0.182
PB2F	99.7	87.2	30.36	0.37	30.73	0.002	0.216
BTP-eC9	93.1	79.9	34.75	0.89	35.64	0.182	/
L8-BO	91.5	77.6	38.00	0.82	38.82	0.472	0.068
PY-IT	94.0	80.4	36.28	0.60	36.88	0.280	0.011
eC9:BO	93.5	80.2	35.08	0.79	35.87	0.234	/

Table S3. Key parameters of contact angle measurements by using water and glycerol droplets.

Film surface	$\gamma_{PM6/X}$ (mN m^{-1})	$\gamma_{BTP-eC9/X}$ (mN m^{-1})	$\gamma_{BTP-eC9:L8-BO/X}$ (mN m^{-1})	ω_x ternary	ω_x quaternary
PM6	/	0.67	0.65	/	/
PB2F	0.02	0.53	0.48	0.76	0.71
BTP-eC9	0.67	/	/	/	/
L8-BO	1.21	0.14	/	-1.60	/
PY-IT	0.71	0.08	0.07	-0.94	-0.98

Table S4. Kinetic fitting parameters according to exciton diffusion and annihilation model.

BTP-eC9:L8-BO	Pump fluence (µJ cm^{-2})	Initial exciton density (×10^{17} cm^{-3})	β (×10^{-7} cm^3 s^{-1})	γ (×10^{-12} cm^3 s$^{-0.5}$)
Fresh film	5	1.97	1.34	9.07
	10	5.05	2.45	7.28
	20	9.64	4.27	4.91
	30	18.47	7.06	1.08
Aged film	5	1.35	1.96	17.55
	10	3.51	3.89	15.34
	20	8.17	6.54	12.52
	30	16.28	12.24	6.80

Table S5. Summary of fitting parameters of temperature-dependent PL linewidths for binary PM6:BTP-eC9 films processed by chloroform and quaternary PM6:BTP-eC9:L8-BO:PY-IT films processed by *o*-xylene before and after photothermal aging.

Active layer	Γ_i (meV)	b (µeV K^{-1})	E_a (meV)
Fresh PM6:BTP-eC9	106.6	297.6	23.8
Aged PM6:BTP-eC9	112.9	351.9	18.3
Fresh PM6:BTP-eC9:L8-BO:PY-IT *o*-XY	103.9	257.2	25.6
Aged PM6:BTP-eC9:L8-BO:PY-IT *o*-XY	106.7	312.7	21.5

Table S6. Kinetic fitting parameters according to the residual charge recombination model.

Active layer	k_T (×10^8 s^{-1})	Aged/fresh k_T (a.u.)	K (×10^8 s^{-1})
Fresh PM6:BTP-eC9	1.99	0.61	147.43
Aged PM6:BTP-eC9	1.21		102.65
Fresh PM6:BTP-eC9:L8-BO:PY-IT	1.49	0.89	122.85
Aged PM6:BTP-eC9:L8-BO:PY-IT	1.32		105.70
Fresh PM6:BTP-eC9:L8-BO:PY-IT *o*-XY	1.53	0.95	119.72
Aged PM6:BTP-eC9:L8-BO:PY-IT *o*-XY	1.46		108.93
Fresh PM6:PB2F:BTP-eC9:L8-BO	1.48	0.88	127.68
Aged PM6:PB2F:BTP-eC9:L8-BO	1.30		108.47
Fresh PM6:PB2F:BTP-eC9:L8-BO *o*-XY	1.51	0.92	124.71
Aged PM6:PB2F:BTP-eC9:L8-BO *o*-XY	1.39		110.39

Table S7. Summary of photovoltaic parameters of the PM6:BTP-eC9-based ternary OSCs with various L8-BO contents under simulated AM 1.5 G illumination at 100 mW cm^{-2}.

Active layer (Weight ratio, solvent)	V_{OC} (V)	J_{SC} (mA cm^{-2})	FF (%)	PCE[a] (%)
PM6:BTP-eC9:L8-BO (1.00:1.20:0.00, CF)	0.851 (0.846±0.005)	27.18 (26.98±0.26)	78.29 (77.88±0.49)	18.11 (17.82±0.27)
PM6:BTP-eC9:L8-BO (1.00:1.15:0.05, CF)	0.854 (0.849±0.006)	27.25 (27.04±0.30)	78.52 (78.13±0.51)	18.27 (17.96±0.30)
PM6:BTP-eC9:L8-BO (1.00:1.10:0.10, CF)	0.855 (0.851±0.004)	27.39 (27.14±0.32)	78.76 (78.39±0.47)	18.44 (18.12±0.29)
PM6:BTP-eC9:L8-BO (1.00:1.05:0.15, CF)	0.857 (0.854±0.005)	27.07 (26.86±0.28)	78.35 (78.02±0.42)	18.18 (17.91±0.25)
PM6:BTP-eC9:L8-BO (1.00:1.00:0.20, CF)	0.857 (0.853±0.006)	26.91 (26.65±0.34)	77.72 (77.35±0.46)	17.92 (17.63±0.28)

[a] The statistical values extracted from ten independent devices.

Table S8. Summary of photovoltaic parameters of the PM6:BTP-eC9-based ternary OSCs with various PY-IT contents under simulated AM 1.5 G illumination at 100 mW cm^{-2}.

Active layer (Weight ratio, solvent)	V_{OC} (V)	J_{SC} (mA cm^{-2})	FF (%)	PCE[a] (%)
PM6:BTP-eC9:PY-IT (1.00:1.20:0.00, CF)	0.851 (0.846±0.005)	27.18 (26.98±0.26)	78.29 (77.88±0.49)	18.11 (17.82±0.27)
PM6:BTP-eC9:PY-IT (1.00:1.17:0.03, CF)	0.855 (0.850±0.007)	27.21 (27.02±0.31)	78.35 (77.94±0.46)	18.23 (17.91±0.30)
PM6:BTP-eC9:PY-IT (1.00:1.15:0.05, CF)	0.857 (0.853±0.006)	27.28 (27.05±0.29)	78.51 (78.02±0.52)	18.35 (18.04±0.28)
PM6:BTP-eC9:PY-IT (1.00:1.13:0.07, CF)	0.856 (0.852±0.005)	26.75 (26.41±0.41)	78.42 (77.98±0.48)	17.96 (17.63±0.32)
PM6:BTP-eC9:PY-IT (1.00:1.10:0.10, CF)	0.855 (0.851±0.006)	26.53 (26.17±0.43)	78.07 (77.63±0.50)	17.71 (17.35±0.34)

[a] The statistical values extracted from ten independent devices.

Table S9. Summary of photovoltaic parameters of the PM6:BTP-eC9:L8-BO-based quaternary OSCs with various PY-IT contents under simulated AM 1.5 G illumination at 100 mW cm^{-2}.

Active layer (Weight ratio, solvent)	V_{OC} (V)	J_{SC} (mA cm^{-2})	FF (%)	PCE[a] (%)
PM6:BTP-eC9:L8-BO:PY-IT (1.00:1.10:0.10:0.00, CF)	0.855 (0.851±0.004)	27.39 (27.14±0.32)	78.76 (78.39±0.47)	18.44 (18.12±0.29)
PM6:BTP-eC9:L8-BO:PY-IT (1.00:1.07:0.10:0.03, CF)	0.860 (0.854±0.007)	27.48 (27.26±0.28)	78.95 (78.67±0.39)	18.66 (18.33±0.31)
PM6:BTP-eC9:L8-BO:PY-IT (1.00:1.05:0.10:0.05, CF)	0.862 (0.857±0.005)	27.55 (27.33±0.35)	79.25 (78.94±0.46)	18.82 (18.53±0.25)
PM6:BTP-eC9:L8-BO:PY-IT (1.00:1.03:0.10:0.07, CF)	0.863 (0.858±0.006)	27.43 (27.20±0.31)	78.62 (78.18±0.49)	18.61 (18.27±0.32)
PM6:BTP-eC9:L8-BO:PY-IT (1.00:1.00:0.10:0.10, CF)	0.859 (0.856±0.007)	27.41 (27.17±0.29)	78.51 (78.05±0.53)	18.49 (18.19±0.28)

[a] The statistical values extracted from ten independent devices.

Table S10. Summary of photovoltaic parameters of the quaternary PM6:BTP-eC9:L8-BO:PY-IT OSCs processed by *o*-xylene with hot spin coatings under simulated AM 1.5 G illumination at 100 mW cm^{-2}.

Active layer (Weight ratio, temperature)	V_{OC} (V)	J_{SC} (mA cm^{-2})	FF (%)	PCE[a] (%)
PM6:BTP-eC9:L8-BO:PY-IT (1.00:1.05:0.10:0.05, 60 °C)	0.847 (0.845±0.007)	26.76 (26.45±0.37)	78.46 (78.15±0.43)	17.78 (17.48±0.28)
PM6:BTP-eC9:L8-BO:PY-IT (1.00:1.05:0.10:0.05, 70 °C)	0.850 (0.848±0.006)	26.88 (26.59±0.34)	78.66 (78.37±0.38)	17.97 (17.69±0.26)
PM6:BTP-eC9:L8-BO:PY-IT (1.00:1.05:0.10:0.05, 80 °C)	0.856 (0.854±0.004)	27.43 (27.25±0.31)	79.16 (78.81±0.42)	18.59 (18.35±0.22)
PM6:BTP-eC9:L8-BO:PY-IT (1.00:1.05:0.10:0.05, 90 °C)	0.858 (0.855±0.005)	27.14 (26.87±0.36)	78.84 (78.49±0.46)	18.36 (18.04±0.30)
PM6:BTP-eC9:L8-BO:PY-IT (1.00:1.05:0.10:0.05, 100 °C)	0.857 (0.854±0.006)	26.98 (26.65±0.41)	78.60 (78.28±0.39)	18.17 (17.83±0.33)

[a] The statistical values extracted from ten independent devices.

Table S11. Summary of photovoltaic parameters of the PM6:BTP-eC9-based ternary OSCs with various PB2F contents under simulated AM 1.5 G illumination at 100 mW cm^{-2}.

Active layer (Weight ratio, solvent)	V_{OC} (V)	J_{SC} (mA cm^{-2})	FF (%)	PCE[a] (%)
PM6:PB2F:BTP-eC9 (1.00:0.00:1.20, CF)	0.851 (0.846±0.005)	27.18 (26.98±0.26)	78.29 (77.88±0.49)	18.11 (17.82±0.27)
PM6:PB2F:BTP-eC9 (0.97:0.03:1.20, CF)	0.851 (0.848±0.006)	27.30 (27.05±0.35)	78.36 (77.92±0.52)	18.21 (17.91±0.28)
PM6:PB2F:BTP-eC9 (0.95:0.05:1.20, CF)	0.858 (0.854±0.005)	27.32 (27.10±0.31)	78.41 (77.94±0.55)	18.39 (18.09±0.26)
PM6:PB2F:BTP-eC9 (0.93:0.07:1.20, CF)	0.856 (0.852±0.007)	26.79 (26.46±0.38)	78.10 (77.63±0.57)	17.91 (17.55±0.34)
PM6:PB2F:BTP-eC9 (0.90:0.10:1.20, CF)	0.853 (0.850±0.006)	26.74 (26.37±0.42)	77.47 (77.06±0.48)	17.67 (17.29±0.36)

[a] The statistical values extracted from ten independent devices.

Table S12. Summary of photovoltaic parameters of PM6:BTP-eC9:L8-BO-based quaternary OSCs with various PB2F contents under simulated AM 1.5 G illumination at 100 mW cm^{-2}.

Active layer (Weight ratio, solvent)	V_{OC} (V)	J_{SC} (mA cm^{-2})	FF (%)	PCE[a] (%)
PM6:PB2F:BTP-eC9:L8-BO (1.00:0.00:1.10:0.10, CF)	0.855 (0.851±0.004)	27.39 (27.14±0.32)	78.76 (78.39±0.47)	18.44 (18.12±0.29)
PM6:PB2F:BTP-eC9:L8-BO (0.97:0.03:1.10:0.10, CF)	0.862 (0.857±0.007)	27.42 (27.18±0.34)	79.07 (78.71±0.45)	18.69 (18.37±0.31)
PM6:PB2F:BTP-eC9:L8-BO (0.95:0.05:1.10:0.10, CF)	0.863 (0.858±0.006)	27.47 (27.26±0.28)	79.18 (78.83±0.42)	18.77 (18.45±0.28)
PM6:PB2F:BTP-eC9:L8-BO (0.93:0.07:1.10:0.10, CF)	0.859 (0.855±0.007)	27.25 (26.95±0.36)	78.29 (77.86±0.52)	18.33 (18.02±0.30)
PM6:PB2F:BTP-eC9:L8-BO (0.90:0.10:1.10:0.10, CF)	0.857 (0.854±0.005)	27.03 (26.68±0.42)	78.08 (77.56±0.55)	18.09 (17.74±0.33)

[a] The statistical values extracted from ten independent devices.

Table S13. Summary of photovoltaic parameters of the quaternary PM6:PB2F:BTP-eC9:L8-BO OSCs processed by *o*-xylene with hot spin coatings under simulated AM 1.5 G illumination at 100 mW cm^{-2}.

Active layer (Weight ratio, temperature)	V_{OC} (V)	J_{SC} (mA cm^{-2})	FF (%)	PCE[a] (%)
PM6:PB2F:BTP-eC9:L8-BO (0.95:0.05:1.10:0.10, 60 °C)	0.852 (0.848±0.006)	26.57 (26.23±0.41)	78.31 (78.03±0.37)	17.73 (17.39±0.32)
PM6:PB2F:BTP-eC9:L8-BO (0.95:0.05:1.10:0.10, 70 °C)	0.854 (0.851±0.004)	26.70 (26.38±0.36)	78.47 (78.18±0.35)	17.89 (17.57±0.29)
PM6:PB2F:BTP-eC9:L8-BO (0.95:0.05:1.10:0.10, 80 °C)	0.859 (0.856±0.005)	27.40 (27.19±0.34)	78.84 (78.58±0.39)	18.56 (18.30±0.24)
PM6:PB2F:BTP-eC9:L8-BO (0.95:0.05:1.10:0.10, 90 °C)	0.861 (0.857±0.004)	27.02 (26.68±0.38)	78.56 (78.27±0.40)	18.28 (17.92±0.33)
PM6:PB2F:BTP-eC9:L8-BO (0.95:0.05:1.10:0.10, 100 °C)	0.858 (0.855±0.005)	26.81 (26.45±0.43)	78.36 (78.08±0.42)	18.17 (17.74±0.40)

[a] The statistical values extracted from ten independent devices.

Table S14. Summary of Photovoltaic parameters for binary and quaternary OSCs.

Active layer	J_{sat} (mA cm^{-2})	J_{ph}* (mA cm^{-2})	J_{ph}# (mA cm^{-2})	P_{diss} (%)	P_{coll} (%)
PM6:BTP-eC9	27.74	27.18	24.58	97.98	88.61
PM6:BTP-eC9:L8-BO:PY-IT	27.85	27.55	25.87	98.92	92.89
PM6:BTP-eC9:L8-BO:PY-IT *o*-XY	27.94	27.43	25.51	98.17	91.30
PM6:PB2F:BTP-eC9:L8-BO	27.93	27.47	25.92	98.35	92.80
PM6:PB2F:BTP-eC9:L8-BO *o*-XY	27.95	27.40	25.46	98.03	91.09

*short-circuit condition, #maximal power output condition, $P_{diss} = J_{ph}*/J_{sat}$, $P_{coll} = J_{ph}#/J_{sat}$.

Table S15. Summary of energy loss parameters for binary and quaternary OSCs.

Active layer	J_0^{rad} (A m^{-2})	qV_{OC}^{rad} (eV)	E_g^{PV} (eV)	qV_{OC} (eV)	E_{loss} (eV)	ΔE_{nonrad} (eV)
PM6:BTP-eC9	4.915×10^{-16}	1.056	1.387	0.851	0.536	0.205
PM6:BTP-eC9:L8-BO:PY-IT	3.743×10^{-16}	1.064	1.391	0.862	0.529	0.202
PM6:BTP-eC9:L8-BO:PY-IT o-XY	4.426×10^{-16}	1.059	1.390	0.856	0.534	0.203
PM6:PB2F:BTP-eC9:L8-BO	3.548×10^{-16}	1.065	1.390	0.863	0.527	0.202
PM6:PB2F:BTP-eC9:L8-BO o-XY	4.106×10^{-16}	1.061	1.390	0.859	0.531	0.202

Table S16. The hole (μ_h) and electron (μ_e) mobility of the PM6:BTP-eC9:L8-BO:PY-IT-based binary and quaternary single-carrier devices before and after photothermal aging.

Active layer	μ_h (×10^{-4} cm^2 V^{-1} s^{-1})	μ_e (×10^{-4} cm^2 V^{-1} s^{-1})	μ_h/μ_e
Fresh PM6:BTP-eC9	7.87±0.23	4.68±0.26	1.68
Fresh PM6:BTP-eC9:L8-BO:PY-IT	8.85±0.19	5.76±0.21	1.54
Fresh PM6:BTP-eC9:L8-BO:PY-IT o-XY	8.59±0.21	5.43±0.25	1.58
Aged PM6:BTP-eC9	4.28±0.28	1.05±0.32	4.08
Aged PM6:BTP-eC9:L8-BO:PY-IT	5.52±0.26	2.23±0.31	2.48
Aged PM6:BTP-eC9:L8-BO:PY-IT o-XY	5.34±0.25	2.19±0.29	2.44

[a] The statistical values extracted from six independent devices.

Table S17. The hole (μ_h) and electron (μ_e) mobility of the PM6:PB2F:BTP-eC9:L8-BO-based binary and quaternary single-carrier devices before and after photothermal aging.

Active layer	μ_h (×10^{-4} cm^2 V^{-1} s^{-1})	μ_e (×10^{-4} cm^2 V^{-1} s^{-1})	μ_h/μ_e
Fresh PM6:BTP-eC9	7.87±0.23	4.68±0.26	1.68
Fresh PM6:PB2F:BTP-eC9:L8-BO	8.56±0.21	5.47±0.24	1.57
Fresh PM6:PB2F:BTP-eC9:L8-BO o-XY	8.28±0.25	5.15±0.27	1.61
Aged PM6:BTP-eC9	4.28±0.28	1.05±0.32	4.08
Aged PM6:PB2F:BTP-eC9:L8-BO	5.27±0.30	2.06±0.34	2.56
Aged PM6:PB2F:BTP-eC9:L8-BO o-XY	5.09±0.26	2.01±0.31	2.53

[a] The statistical values extracted from six independent devices.

Table S18. Gaussian fitting results of trap states for PM6:BTP-eC9:L8-BO:PY-IT-based binary and quaternary OSCs with different solvent treatments before and after photothermal aging.

Active layer	N_t (×10^{17} cm^{-3} eV^{-1})	σ (meV)	E_t (meV)
Fresh PM6:BTP-eC9	0.67	22	147
Fresh PM6:BTP-eC9:L8-BO:PY-IT	0.44	18	147
Fresh PM6:BTP-eC9:L8-BO:PY-IT o-XY	0.46	19	147
Aged PM6:BTP-eC9	2.50	27	153
Aged PM6:BTP-eC9:L8-BO:PY-IT	1.58	24	152
Aged PM6:BTP-eC9:L8-BO:PY-IT o-XY	1.03	21	151

Table S19. Gaussian fitting results of trap states for PM6:PB2F:BTP-eC9:L8-BO-based binary and quaternary OSCs with different solvent treatments before and after photothermal aging.

Active layer	N_t (×10^{17} cm^{-3} eV^{-1})	σ (meV)	E_t (eV)
Fresh PM6:BTP-eC9	0.67	22	147
Fresh PM6:PB2F:BTP-eC9:L8-BO	0.53	20	147
Fresh PM6:PB2F:BTP-eC9:L8-BO *o*-XY	0.54	21	147
Aged PM6:BTP-eC9	2.50	27	153
Aged PM6:PB2F:BTP-eC9:L8-BO	1.64	25	152
Aged PM6:PB2F:BTP-eC9:L8-BO *o*-XY	1.23	23	151

Table S20. Summary of GIWAXS (010) π-π stacking peak information in the OOP direction.

Sample	$q_{z(010)}$ (nm^{-1})	*d*-spacing (nm)	FWHM (nm^{-1})	CCL (nm)
PM6	16.90	0.372	2.52	2.24
PB2F	16.92	0.371	2.38	2.38
L8-BO	17.75	0.354	2.07	2.74
BTP-eC9	17.54	0.358	2.31	2.45
PY-IT	16.53	0.380	2.16	2.62
PB2F:BTP-eC9	17.55	0.358	2.26	2.50
PM6:L8-BO	17.46	0.360	2.21	2.56
PM6:PY-IT	16.74	0.375	2.19	2.58
Fresh PM6:BTP-eC9	17.59	0.357	2.15	2.63
Aged PM6:BTP-eC9	17.62	0.357	2.37	2.39
Fresh PM6:BTP-eC9:L8-BO:PY-IT	17.55	0.358	2.02	2.80
Aged PM6:BTP-eC9:L8-BO:PY-IT	17.59	0.357	2.21	2.56
Fresh PM6:BTP-eC9:L8-BO:PY-IT *o*-XY	17.55	0.358	2.05	2.75
Aged PM6:BTP-eC9:L8-BO:PY-IT *o*-XY	17.51	0.359	2.13	2.66
Fresh PM6:PB2F:BTP-eC9:L8-BO	17.54	0.358	1.99	2.84
Aged PM6:PB2F:BTP-eC9:L8-BO	17.57	0.358	2.14	2.65
Fresh PM6:PB2F:BTP-eC9:L8-BO *o*-XY	17.52	0.359	2.03	2.79
Aged PM6:PB2F:BTP-eC9:L8-BO *o*-XY	17.49	0.359	2.11	2.68

4. Supplementary References

1. R. Tadmor, *Langmuir*, 2004, **20**, 7659-7664.

2. D. Li and A. Neumann, *J. Colloid Interface Sci.*, 1990, **137**, 304-307.

3. M. Sumita, K. Sakata, S. Asai, K. Miyasaka and H. Nakagawa, *Polym. Bull.*, 1991, **25**, 265-271.

4. C. Daniel, L. M. Herz, C. Silva, F. J. M. Hoeben, P. Jonkheijm, A. P. H. J. Schenning and E. W. Meijer, *Phys. Rev. B*, 2003, **68**, 235212.

5. P. Jia, L. Qin, D. Zhao, Y. Tang, B. Song, J. Guo, X. Li, L. Li, Q. Cui, Y. Hu, Z. Lou, F. Teng and Y. Hou, *Adv. Funct. Mater.*, 2021, **31**, 2107125.

6. H. Yin, L. Ma, Y. Wang, J. Huang, H. Yu, J. Zhang, P. C. Y. Chow, W. Ma, S. K. So and H. Yan, *Adv. Mater.*, 2019, **31**, 1903998.

7. H. Yin, K. L. Chiu, P. Bi, G. Li, C. Yan, H. Tang, C. Zhang, Y. Xiao, H. Zhang, W. Yu, H. Hu, X. Lu, X. Hao and S. K. So, *Adv. Electron. Mater.*, 2019, **5**, 1900497.

8. Z. Zhang, Y. Li, G. Cai, Y. Zhang, X. Lu and Y. Lin, *J. Am. Chem. Soc.*, 2020, **142**, 18741-18745.

9. J. Zhou, D. He, Y. Li, F. Huang, J. Zhang, C. Zhang, Y. Yuan, Y. Lin, C. Wang and F. Zhao, *Adv. Mater.*, 2023, **35**, 2207336.

10. S. Khelifi, K. Decock, J. Lauwaert, H. Vrielinck, D. Spoltore, F. Piersimoni, J. Manca, A. Belghachi and M. Burgelman, *J. Appl. Phys.*, 2011, **110**, 094509.

11. B. Fan, X. Du, F. Liu, W. Zhong, L. Ying, R. Xie, X. Tang, K. An, J. Xin, N. Li, W. Ma, C. J. Brabec, F. Huang and Y. Cao, *Nat. Energy*, 2018, **3**, 1051-1058.

12. L. Ye, K. Weng, J. Xu, X. Du, S. Chandrabose, K. Chen, J. Zhou, G. Han, S. Tan, Z. Xie, Y. Yi, N. Li, F. Liu, J. M. Hodgkiss, C. J. Brabec and Y. Sun, *Nat. Commun.*, 2020, **11**, 6005.

13. Y. Wang, D. Qian, Y. Cui, H. Zhang, J. Hou, K. Vandewal, T. Kirchartz and F. Gao, *Adv. Energy Mater.*, 2018, **8**, 1801352.

14. Y. Liang, D. Zhang, Z. Wu, T. Jia, L. Lüer, H. Tang, L. Hong, J. Zhang, K. Zhang, C. J. Brabec, N. Li and F. Huang, *Nat. Energy*, 2022, **7**, 1180-1190.

15. S. Li, R. Zhang, M. Zhang, J. Yao, Z. Peng, Q. Chen, C. Zhang, B. Chang, Y. Bai, H. Fu, Y. Ouyang, C. Zhang, J. A. Steele, T. Alshahrani, M. B. J. Roeffaers, E. Solano, L. Meng, F. Gao, Y. Li and Z. G. Zhang, *Adv. Mater.*, 2023, **35**, 2206563.

16. K. An, W. Zhong, F. Peng, W. Deng, Y. Shang, H. Quan, H. Qiu, C. Wang, F. Liu, H. Wu, N. Li, F. Huang and L. Ying, *Nat. Commun.*, 2023, **14**, 2688.

17. B. Liu, H. Sun, J. W. Lee, Z. Jiang, J. Qiao, J. Wang, J. Yang, K. Feng, Q. Liao, M. An,

B. Li, D. Han, B. Xu, H. Lian, L. Niu, B. J. Kim and X. Guo, *Nat. Commun.*, 2023, **14**, 967.

18. S. Li, C. He, T. Chen, J. Zheng, R. Sun, J. Fang, Y. Chen, Y. Pan, K. Yan, C.-Z. Li, M. Shi, L. Zuo, C.-Q. Ma, J. Min, Y. Liu and H. Chen, *Energy Environ. Sci.*, 2023, **16**, 2262-2273.

19. Z. Ge, J. Qiao, Y. Li, J. Song, C. Zhang, Z. Fu, M. H. Jee, X. Hao, H. Y. Woo and Y. Sun, *Adv. Mater.*, 2023, 2301906, DOI: 10.1002/adma.202301906.

20. B. Fan, W. Zhong, W. Gao, H. Fu, F. R. Lin, R. W. Y. Wong, M. Liu, C. Zhu, C. Wang, H. L. Yip, F. Liu and A. K. Jen, *Adv. Mater.*, 2023, 2302861, DOI: 10.1002/adma.202302861.

21. B. Fan, W. Gao, R. Zhang, W. Kaminsky, F. R. Lin, X. Xia, Q. Fan, Y. Li, Y. An, Y. Wu, M. Liu, X. Lu, W. J. Li, H. L. Yip, F. Gao and A. K. Jen, *J. Am. Chem. Soc.*, 2023, **145**, 5909-5919.

22. R. Sun, T. Wang, Q. Fan, M. Wu, X. Yang, X. Wu, Y. Yu, X. Xia, F. Cui, J. Wan, X. Lu, X. Hao, A. K. Y. Jen, E. Spiecker and J. Min, *Joule*, 2023, **7**, 221-237.

23. Y. Wang, J. Luke, A. Privitera, N. Rolland, C. Labanti, G. Londi, V. Lemaur, D. T. W. Toolan, A. J. Sneyd, S. Jeong, D. Qian, Y. Olivier, L. Sorace, J.-S. Kim, D. Beljonne, Z. Li and A. J. Gillett, *Joule*, 2023, **7**, 810-829.